POLITEHNICA UNIVERSITY OF BUCHAREST

Doctoral School in Engineering and Applications of Lasers and Accelerators

Decision No. ____ from_____

Ph.D. THESIS SUMMARY

Andreea Bianca ȘERBAN (GHERGHE)

NOI MATERIALE PENTRU MODERAREA DE POZITRONI

NEW MATERIALS FOR POSITRON MODERATION

THESIS COMMITTEE

CS I Dr. Ing. Alexandru Călin Ur Politehnica Univ. of Bucharest & ELI-NP	President
Prof. Dr. Dimiter Lukanov Balabanski Politehnica Univ. of Bucharest & ELI-NP	PhD Supervisor
CS II Dr. habil. Nikolay Ivanov Djourelov Politehnica Univ. of Bucharest & ELI-NP	Referee
CS I Dr. habil. Cristian Mihail Teodorescu University of Bucharest & NIMP	Referee
Prof. Dr. Patrick Nédélec Université Lyon 1 (UCBL) & Institut de Physique des 2 Infinis (IP2I)	Referee

BUCHAREST 2023

Acknowledgements

I would like to take advantage of this opportunity to express my deepest thanks to my supervisor, Dr. Dimiter Balabanski, for his unwavering support and encouragement during the course of my work on the thesis. I am thankful beyond words for having been able to learn from him. In addition, I would not have been able to make any headway on this path if the advising committee, which consisted of Dr. Nikolay Djourelov, Dr. Victor Leca, and Dr. Cristian Teodorescu, had not offered me unreserved and consistent assistance in the form of advice and support. Without it, I would not have been able to make any progress. This adventure would not have been possible for me to finish if it were not for their assistance.

I would like to express my great appreciation to the Target Laboratory group and Positron Laboratory group, in particular to the heads of the laboratories, and to Doru Dinescu, Cristina Gheorghiu, Iulia Zai, Daniel Popa, Ionela Iliescu, Marcel Conde, and Aurelia Ionescu for their intellectual support related to the experimental parts of the thesis and for their invaluable patience and feedback. Also, great support was offered by the people from University Politehnica of Bucharest from the Department of Science and Engineering of Oxide Materials and Nanomaterials, especially Vladimir Lucian Ene, Ionela Neacsu, Bogdan Vasile, and others, who helped me to overcome challenges and given advice on drawing up the work competently. I would like to extend my sincere thanks to my Gamma Driven Experiments Department colleagues, mostly to my office colleagues who taught me valuable science and life lessons. Last but not least, I would like to acknowledge the help of the ELI-NP, ICPE-CA and IFIN-HH personnel that made big efforts for helping me to accomplish the results included in this thesis.

I would be negligent if I did not mention my treasured friends and family, most notably my brother Nicolae, my parents Anisoara and Ion, my husband Marian, and my cherished son Theo. Their confidence in me served as a driving force for me throughout the whole of this process.

Table of Contents

List of figures ..... **v**

List of tables ..... **vii**

Chapter 1 Introduction **1**

A. Scientific motivation 2

B. Structure of the thesis. 3

Chapter 2 Theoretical aspects **5**

2.1 Positron sources. Positron moderators 5

2.2 Nitride- and oxide-based materials. Crystal defects 8

2.3 Thin film deposition. Magnetron sputtering 11

Chapter 3 Moderator. Fabrication and characterization **13**

3.1 Experimental setup 14

3.2 A short introduction to the characterization methods. 15

3.3 Gallium nitride deposition 18

3.4 Buffer layer 20

3.4.1 Aluminum nitride (AlN) 20

3.4.2 Zinc oxide (ZnO) 21

3.4.3 Titanium nitride (TiN) 21

3.5 Summary 22

Chapter 4 Studies on commercially available GaN samples **23**

4.1 Materials and Methods 23

4.2 Results and Discussion 24

4.3 Summary 26

Chapter 5 Optimization and manufacture of the positron moderation device based on a magnetic bottle **27**

5.1 The magnetic bottle device concept. 28
5.1.1 Ideal positron magnetic bottle 28
5.1.2 Design limitations. Fast positron source and moderator 29
5.2 Numerical simulations procedure 30
5.3 Numerical simulations results 31
5.4 Manufacturing of the positron moderation device 34
5.4.1 Magnetic coils construction 34
5.5 Designing and assembling the experimental setup 34
5.5.1 Ti foils irradiation 35
5.5.2 W annealing 35
5.6 Results 36
5.7 Summary 37
Chapter 6 Conclusions and perspectives 39
Bibliography 41

List of figures

Figure 1 The equipment's layout of the ELI-NP Positron Spectroscopy laboratory 2

Figure 2.1 The FA moderation schematic diagram of a silicon moderator from ref. [33]. The positron thermalizes to a position (r, θ) in 10 ps at an implantation depth of $x = r\cos\theta$. It then follows the direction of the applied E-field, eventually reaching a thin epitaxial silicide contact (20 Å) and being emitted in vacuum..... 7

Figure 2.2 Development of a magnetic bottle trap device of Gerchow et *al.* [18], designed with two Ti irradiated foils (*source*), a W (110) foil illustrated as *moderator*, and a extraction grid placed inside a magnetic bottle. The positrons are confined and lose their energy by multiple passes through the moderator foils. The extraction grid is kept at ground potential in order to maximize the moderated positron efficiency 8

Figure 2.3 Growth modes. (a)Volmer-Weber growth; (b)Stranski-Krastanov growth; (c) Frank-van der Merwe growth [43] 9

Figure 2.4 Several types of lattice defects [46]..... 10

Figure 2.5 Schematic of magnetron sputtering process 12

Figure 3.1 Step-by-step diagram showing the fabrication of the positron moderator based on GaN film 14

Figure 3.2 Summary of various signals obtained by electron interaction with matter..... 16

Figure 3.3 Diagram of photoelectric effect in XPS..... 17

Figure 3.4 AFM images of the GaN films with different thickness growth on Al_2O_3 substrate (a) thin film, (b) thick film..... 19

Figure 3.5. XRD 2theta scans for the AlN layers grown on Si substrates 20

Figure 3.6 XRD 2theta scans for the ZnO layers grown on Si substrates..... 21

Figure 3.7 XRD 2theta scan of ST4 showing TiN (200) 22

Figure 4.1 Plotted depth profiles $S(E_+)$ of GaN/SiC. The experimental errors are in the order of the experimental point size. The stairs represent the best parameters obtained by the fit of a 4-layer model to the experimental data by the VEPFIT software. The values represent the cumulative thickness of the layers. The upper part of figure is the experimental data and the best fit of the relative Ps fraction, $F_{Ps}(E_+)$ 25

Figure 5.1 Sectional diagram of the magnetic bottle device showing a chamber with two coils functioning as magnetic mirrors and a transport tube [87] 29

Figure 5.2 Moderated positrons spot for the coils' configuration L10w7 under magnetic guiding Bzt = 100 G inside the transport solenoid. The white circle marks the central ⌀10 mm area [87] 31

Figure 5.3 Fraction of the total and "useful" detected moderated positrons together with B_{max} in the case of coils' configuration presented in Table 5.1 [87] 32

Figure 5.4 Simulated z-axis position of positrons from 1-µm-thick ^{48}V implanted in 1-µm-thick W [87] 32

Figure 5.5 Simulated total moderated e^+ fraction and estimated initial slow e^+ intensity for 8-h-activation of the source foil as a function of thickness of the source foil [87] 33

Figure 5.6 Simulated total moderated e^+ fraction as a function of thickness of the moderation foil in cases of source foil thickness 1 and 10 µm [87] 33

Figure 5.7 Vacuum chamber and magnets assembled together. Magnetic field measuring axes 34

Figure 5.8 Magnetic bottle experimental setup with analysis cross equipped with two $CeBr_3$detectors. 35

Figure 5.9 Magnetic bottle chamber assembled together with the frame 37

List of tables

Table 2.1 Basic parameters of some advanced semiconductors..... 9

Table 4.1. Total defect densities, defect correlation lengths and effective positron diffusion lengths in GaN, where d is the layer thickness, ρdt is the total threading dislocation density, r_d is the mean distance between two dislocations, L is the defect correlation length (edge and screw) and L_{eff} is the effective positron diffusion length 26

Table 5.1 Outer radius, coil thickness, windings per coil, maximum current, and total conductor length are calculated. The additional insulation surrounding the conductors is included (0.5 mm) in the coil's diameter and thickness. Maximum coil current must be lower than the power supply's maximum current [97] 30

Chapter 1

Introduction

Positrons are used in many research and industrial fields due to their fast and wide range of energy distribution. One of the most important aspects of their use is the creation of low-energy, slow positron beams (monoenergetic). These beams can be generated by decreasing the energy of β+ particles to a few electron volts using the so-called moderators. A high value of moderation efficiency defined as the ratio between the number of thermal positrons released by the moderator and the number of high-energy positrons provided to the moderator is an essential requirement. Rare gas solids, such as Ne and Ar, have the highest moderation efficiencies (7×10^{-3}), but they are difficult to manipulate and the positron beam cross-section is not as narrow as when a metallic moderator is used. Tungsten is the most effective metal moderator, with an approximate 3×10^{-3} moderation efficiency [1]. A critical requirement for a material to be positron moderator is its work function for positrons, Φ_+, to be negative. For example, Φ_W+= - 3.0 eV [2], [3] for tungsten and Φ_{Pt}+= -1.95 eV [4] for platinum.

The semiconductors with wide band gaps are attractive for use as positron moderators because they can absorb and slow down positrons effectively due to their high atomic mass and dense atomic structure. For instance, GaN and 6H-SiC have work function values of - 2.4 ± 0.3 eV and −3.0 ± 0.2 eV respectively [5], [6].

A. Scientific motivation

The high intensity and high brightness gamma-ray beam that is planned to be produced at ELI-NP as a result of inverse Compton scattering is expected to be an essential research tool. To avoid material activation issues, only beam operated at low energy will be employed for slow e^+ generation. A new slow positron beam line is under development with three spectroscopic experimental measurement stations as shown in Figure 1 [7]. Positron Annihilation Lifetime Spectroscopy (PALS) is a powerful technique for detecting defects and determining the size (type) and relative concentrations of open volume defects [8]. The coincidence Doppler Broadening Spectrometer (CDBS) consists of two pairs of HPGe detectors, arranged to detect in time and energy coincidence conditions for the 511 keV annihilation γ-rays [9]. The information obtained is vital for determining the type of defects that are present in metals and semiconductors [10], [11].

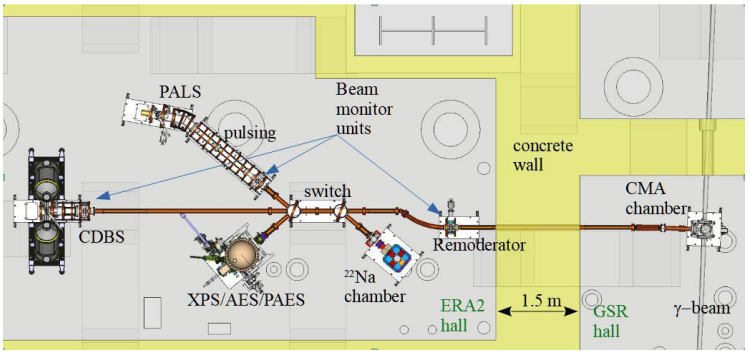

Figure 1 The equipment's layout of the ELI-NP Positron Spectroscopy laboratory

Age MOmentum Correlation (AMOC) is designed to allow the HPGe detectors to be moved to the PALS beamline, and for each of them to be set to operate in timing coincidence with the fast BaF_2 detector aligned in an anti-collinear direction [12]. Positron induced Auger Electron Spectroscopy (PAES), the complementary technique to Electron induced Auger Electron Spectroscopy (AES), can be used to investigate the atomic layer of a surface that is exactly the surface's topmost layer [13], [14]. As Figure 1 shows, the positron beam created using the gamma beam will be moderated through the converter/moderator assembly (CMA) made of tungsten or platinum [15]. Considering that gamma beam time will be limited by other nuclear physics experiments, the round-year operation solution of

the laboratory will be to feed the beamlines with e^+ obtained from a commercial ^{22}Na source. Irrespective of the method by which it was created, for modification of the positron energy, a moderator is required. For this purpose, a solid-state moderator must fulfill numerous requirements for the structure, but at the same time, it must be able to have a range of compositions, each of which produces a distinct negative work function. Studies have shown that positron diffusion length is between 200 and 300 nm in ideal lattice semiconductors, and that an electric field can increase the number of positrons that reach the surface [16].

GaN, a semiconductor with a bandgap energy of 3.44 eV, is being considered for use as a solid moderator in this project. Its α-hexagonal wurtzite structure demonstrates the realistic capability of crystal growth in favored directions, with a minimal lattice misfit in comparison to typical substrates (Si, Al_2O_3, SiC) [16],[17]. Experimental research on GaN has shown a positron work function of 2.4 ± 0.3 eV, a positron branching ratio of 0.48 ± 0.02 on the surface, and a positron diffusion length of 19.3 ± 1.4 nm [6], making it a suitable positron moderator.

This work was motivated by the desire to build a new form of transmission or reflection mode moderator or a field-assisted (FA) moderator. To create novel materials for positron moderation, high crystal quality and very low defect and impurity concentrations are necessary. The moderator conversion efficiency is an important factor, and this study involves the optimization of a magnetic bottle trap in which fast positrons are captured and can interact several times with the moderator material.

B. Structure of the thesis.

In the introduction chapter, there is a concise summary of the work's purpose and structure, as well as an explanation of its methodology.

In the second chapter, there is an introduction to the fundamentals of positron sources and an explanation of the roles that moderators play in the performance of the positron beams by using these sources. In addition, the nitride and oxide semiconductors, as well as the crystal defects, are discussed there. And last, towards the end of the chapter, an introduction to magnetron sputtering deposition as well as an

outline of the techniques that are used to grow materials through deposition processes is provided.

The manufacturing and characterization of the GaN as a first layer when it is deposited to the substrate is presented in Chapter 3. A general summary of the target's characterization and the correlation with the samples that were grown is presented here. The following section of this chapter is dedicated to the deposition and characterization of the various materials that can be used as buffer layers.

In Chapter 4, analysis of positron data is provided alongside the results of an investigation of some GaN epitaxially produced samples.

In Chapter 5 a comprehensive discussion on the optimization and production of a positron moderation device that is based on a magnetic bottle is provided. In this section, the experiment that was conducted by Gerchow *et al*. [18] is fallowed in order to provide an overview of the optimized device. In addition, the development of the magnetic coils that support the magnetic bottle, the design of the chamber, the construction of the experimental setup, the irradiation of the foils, the annealing of the moderator, and the results of the experiments are discussed.

A summary of the study, including its results and perspectives, is offered in the last chapter of the document.

Chapter 2

Theoretical aspects

2.1 Positron sources. Positron moderators

The most commonly used β+ sources in positron spectroscopy are ^{22}Na, ^{58}Co, ^{64}Cu and ^{68}Ga [19]. The most recent study is centered on the development of high-intensity, slow positron beams by producing electron-positron pairs using powerful gamma rays. Pairs are created by the interaction of gamma rays with energies larger than 1022 keV with the electrical field of the nucleus or, although the chance is minimal, with that one of an electron [20]. The sole difference in the notion of positron generation through pair formation is the mechanism for producing high-energy gamma rays. Neutron-induced Positron source MUniCH (NEPOMUC) in Germany is the most powerful positron source in the world. It uses the nuclear reaction ^{113}Cd (n, γ)^{114}Cd to create high-energy gamma quanta after thermal neutron capture [21]–[23]. At contrast to NEPOMUC, the research reactor in Delft, Netherlands, exploits the flow of gamma radiation produced by the fission process at the nuclear reactor's core [24]. The third and most commonly used technique is the LINAC-based positron source, which employs high-energy bremsstrahlung radiation to form an electron-positron pair in a high-Z material [25], [26].

Positrons may also be generated by gamma beams with high energy, which are produced by the inverse Compton scattering of photons with electrons [15], [27]. This is yet another method of producing positrons that is planned to be implemented at Extreme Light Infrastructure - Nuclear Physics (ELI - NP) facility located in Romania [15].

A material (convertor) having a high nuclear charge Z, such as W, Ta, or Pt, is required for the gamma-positron-electron pair conversion to efficiently take place. The cross section, ($\sigma_{e^-e^+}$) dependance is as follows:

$$\sigma_{e^-e^+} = Z^2 f(E_\gamma, Z), \quad 2.1$$

where $f(E_\gamma, Z)$ is a function that depends on the energy of the gamma ray (E_γ) and the atomic number of the target material.

Thus, the probability of pair formation is direct proportional with gamma's energy, $E\gamma$, and the squared atomic number of the material, but as observed in the experimental setup planned in the Ref. [15] and optimized as described in Ref. [28], at high Z values, the cross section and by default the e^-e^+ creation increase, but the positron moderation efficiency decreases. Therefore, for the optimum slow positron production the Convertor-Moderator Assembly (CMA) follows the compromise between the geometric design and the choice of the moderation material. It is desired that the emphasis of this effort be placed on monoenergetic positron beams within the scope of this research. It is important to note that the terms slow, moderated, or low-energy positron beam is used synonymously with the phrase monoenergetic slow positron beam [20]. Monoenergetic positron beams are used to differentiate between the information contributed by the surface/subsurface and the bulk, allowing for the study of layers that are just a few tens of nanometers thick and certain surface properties.

The process by which positrons interact in a volume of gas or of a solid is similar. The fundamental difference is that in gases no excitation of collective modes such as plasmons or phonons exist because of the lack of long-range correlation. Pending the development of sustainable materials for moderation, experiments were carried out with coated foils, as well as with other materials and geometries, as described in [29]–[31].

Besides the criteria mentioned in the Introduction, in the case of semiconductor materials, the moderation can be improved by an applied electric field, which gives a drift velocity to the positrons. This FA moderation is based on the idea that the thermalized positrons will be moved into the vacuum interface and emitted spontaneously [32]. The diffusion equation was solved by Beling *et al.*[33] for a Si moderator (see Figure 2.1), and they obtained formulas for the fraction of positrons that drift from the barriers placed at $x = 0$ and $x = d$. In the situation of a high electric field, when the drift velocity is $v(E) \gg \sqrt{D^+\tau}$, where D^+ is the positron diffusion constant, and τ represents the positron lifetime, thus $\sqrt{D^+\tau}$ represents the positron diffusion coefficient, the diffusive components may be ignored, and the equation that describes the e^+ fraction that reaches $x = d$ is as follows:

$$x(d) = \frac{\tau\alpha v(E)e^{\alpha d} - e^{\frac{-d}{v(E)\tau}}}{1-\tau\alpha v(E)} \quad . \qquad 2.2$$

Schematic representation of the positron implantation profile used in the theoretical calculations for FA moderation is presented in Figure 2.1. The positron that was thermalized at the position (r, θ), represented by the depth $x = r\cos\theta$, within 10 ps follows the direction of the applied *E*-field, eventually reaching a thin epitaxial silicide contact (20 Å) and being emitted in vacuum.

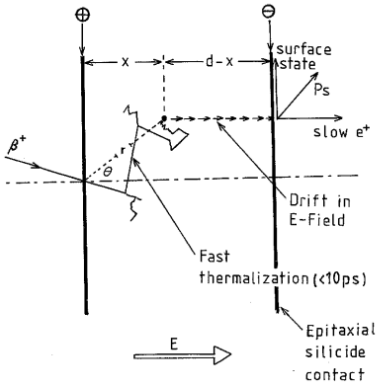

Figure 2.1 The FA moderation schematic diagram of a silicon moderator from ref. [33]. The positron thermalizes to a position (r, θ) in 10 ps at an implantation depth of $x = r\cos\theta$. It then follows the direction of the applied E-field, eventually reaching a thin epitaxial silicide contact (20 Å) and being emitted in vacuum

Finally, Beling *et al.*[33] proved that FA-Si present many advantages, one being the self-supporting into the vacuum. Also, they showed that a silicide ($NiSi_2$, PtSi,

etc.) layer can be used to facilitate the contacts for the electric field. Some years after, a theoretical research was undertaken by Beling *et al.* [34] where they established that positron emission is favored by some semiconductors as GaN, GaP, ZnSe, SiC, *etc.*

Experiments in electric and magnetic fields were also carried out with the goal of improving the positron moderation efficiently [35]–[37]. Gerchow *et al.* [18] published the development of an magnetic bottle trap that improve the W moderation efficiency by 1.8(2)%. The design of the magnetic bottle device is shown in Figure 2.2. This device is based on the idea that fast positrons from a source are captured by the magnetic field and undergo multiple passes through the source and moderator foils thus increasing the chance to be moderated.

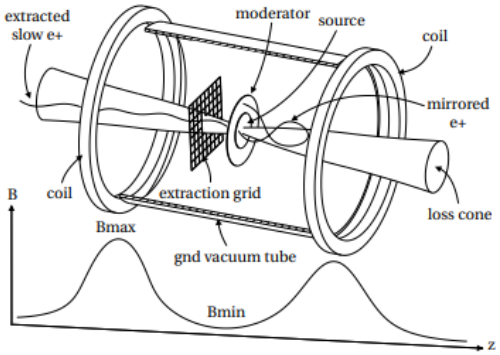

Figure 2.2 Development of a magnetic bottle trap device of Gerchow et *al.* [18], designed with two Ti irradiated foils (*source*), a W (110) foil illustrated as *moderator*, and a extraction grid placed inside a magnetic bottle. The positrons are confined and lose their energy by multiple passes through the moderator foils. The extraction grid is kept at ground potential in order to maximize the moderated positron efficiency

2.2 Nitride- and oxide-based materials. Crystal defects.

After the invention of the transistor in 1948 [38], interest in the development of silicon technology grew along with the success of electronics. Nevertheless, nitride and oxide semiconductors have gained importance due to the enormous demands on their specific properties. An essential reason for this interest is the direct wide bandgap (0.7 eV InN, 3.4 eV GaN, 6.2 eV AlN [39], [40]) continuously tunable

by changes in the doping concentration. Table 2.1 summarizes some of the properties of these materials and their crystal structure.

Table 2.1 Basic parameters of some advanced semiconductors

Structure	AlN	InN	GaN	ZnO	TiN
a [Å] / *c* [Å]	3.112/4.982	3.548/5.760	3.189/5.185	3.2495/5.2069	4.241
Density [g/cm^3]	3.255	6.81	6.095	5.606	5.21
Melting Point [^{o}C]	2500	1100	1600	1974	2947
band gap [eV]	6.2	0.7	3.4	3.3	3.4
Crystal structure	wurtzite	wurtzite	wurtzite	wurtzite	cubic

The growth of nitride/oxide semiconductors is a challenge due to the technical provocation linked to the processing and growth of these materials. The first steps are to choose the material and transport it over the chosen substrate. Subsequent to that is the particles condensation. Contaminants, crystal structure, etc. of the substrate surface directly influence the deposition rate. There are three different types of growth modes for thin films [41], [42], which are represented in Figure 2.3.

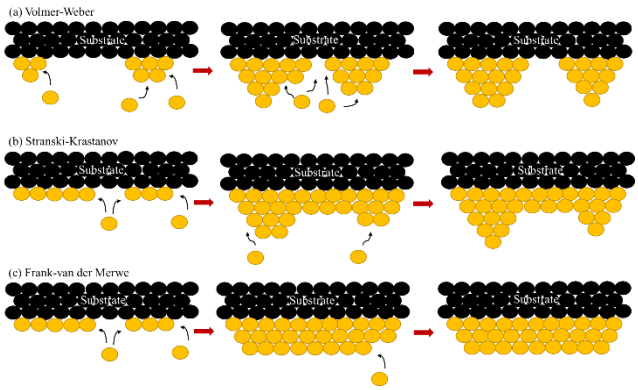

Figure 2.3 Growth modes. (a)Volmer-Weber growth; (b)Stranski-Krastanov growth; (c) Frank-van der Merwe growth [43]

The final physical and chemical properties of the new material growth are strongly influenced by the chosen substrate. The film-substrate mismatch parameter is the first criterion, and substrates with substantial discrepancies in the physical

properties increase the threading dislocation concentration, the stress of the growth layers, and the misfit. A.Kukushkin *et al*. review the most used substrates for GaN epitaxy [44], and reported an asymmetry around 16% between sapphire and gallium nitride, a thermal conductivity coefficient of 0.25 Wt/cmK at 100 ºC, a high concentration of dislocations of the mismatch ($10^{10}cm^{-2}$), and a biaxial compressive strain that arises upon cooling due to the thermal expansion coefficient of Al_2O_3 which is higher than that of GaN. Nitridization of the Si substrate surface leads to a significant decrease in dislocation density, and deposition of a few Al monolayers as a buffer after nitridization decreases the nitridization barrier [44].

Defects, as induced in the deposition process, are the arrangement of atoms that contain imperfections that have a profound effect on the property's behavior of the materials as seen in Figure 2.4. These defects can be categorized into 0-dimensional defects (0D) or point defects, line defects (1D), plane defects (2D), grain boundary, twin boundary, stacking faults, and volume defects (3D). Edge dislocation is a type of line defect in crystal lattices in which the defect results from either the presence of another atomic plane or the loss of half an atomic plane in the middle of the lattice. When stress is applied to a crystal with this defect, the dislocation area moves parallel to the direction of the stress, but the motion in the region where one half of an atomic plane occurs is extremely slight compared to the region where the other half of that atomic plane is absent. This defect can glide in any plane [45].

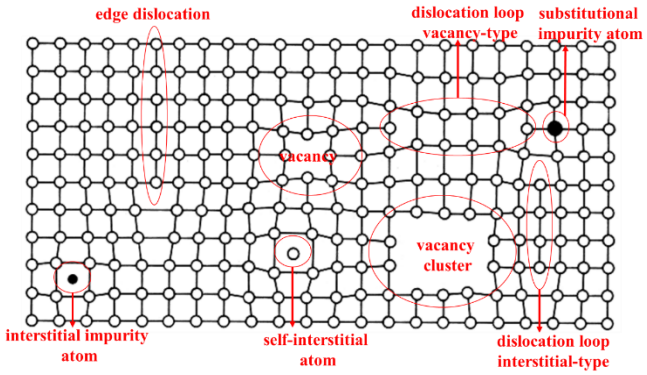

Figure 2.4 Several types of lattice defects [46]

The other type of line defect is screw dislocation that occurs when the planes of atoms in the crystal lattice follow a helical path around the dislocation line. Unlike an edge dislocation, when stress is applied on a crystal containing this defect, the dislocation area moves perpendicular to the direction of stress. However, the stress

caused by screw dislocations is comparatively less complex than that of edge dislocations.

2.3 Thin film deposition. Magnetron sputtering

The thin film research field has developed various methods of deposition and growth, which can be classified as physical and chemical processes. The first includes physical vapor deposition (PVD) such as sputtering, laser ablation, etc., whilst chemical vapor deposition (CVD) such as metal-organic deposition, etc. is part of the chemical process.Via the PVD method, thin films are grown by condensing on the substrate surface the evaporated material from a target material. Nowadays, some of the commonly used methods to grow GaN are metal-organic vapor-phase epitaxy (MOVPE) [47], Molecular Beam Epitaxy (MBE) [48], and magnetron sputtering [49]. Magnetron sputtering is the PVD method applied for thin film deposition described in this research thesis. Gaseous plasma is used to erode the surface of the target, followed by the movement of atoms through the vacuum and their deposition on the substrate.

Magnetron sources were created in the 1970s and are a considerable efficiency improvement for the sputtering technique. Strong magnetic fields, mostly from permanent magnets, are used to restrict secondary electrons near the target surface, leading to a stronger ionization of the sputter-gas atoms, a higher deposition rate, and dense plasma [50]. The strong electric field generated by applied voltage at the cathode in a magnetron sputter source accelerates secondary electrons in the direction normal to the target surface. The magnetic field is designed to align in a direction parallel to the surface of the target, as shown in Figure 2.5, causing electrons to move in cycloidal trajectories. This leads to an increase in plasma currents and collisional ionization of the sputter-gas atoms, which condense on a substrate as a thin film.

Direct current (DC), pulsed DC, radio frequency (RF), and high-power impulse magnetron sputtering are some of the modes that can be operated to get the best possible outcomes. Additionally, a reactive gas (nitrogen, oxygen, hydrocarbons, sulfur, etc.) can be added to the plasma, which then goes through a chemical reaction

before depositing on the sample. This process is known as reactive sputtering, and it enables the production of a compound between the target material and the reactive gas.

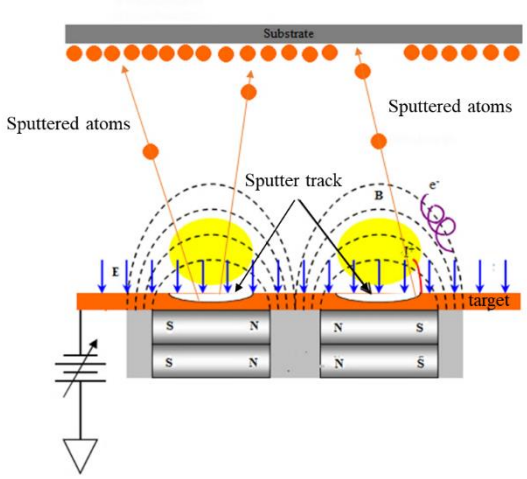

Figure 2.5 Schematic of magnetron sputtering process

Chapter 3

Moderator. Fabrication and characterization

The goal to create a novel transmission or reflection mode moderator or a field-assisted, FA, moderator drove this research. A full scheme of the steps followed during the research described in this thesis in Figure 3.1. Current publications on the production of GaN films reveal that heteroepitaxial GaN films are developed on a variety of substrates [51], [52]. Particularly, chosen substrates for this research are Si, TiO_2, ZnO, and Al_2O_3. Prior to the deposition, the substrates were ultrasonically cleaned through 10 min baths in isopropanol, acetone, and ultrapure water, annealed at 700 ^oC, and investigated by different techniques, such as X-ray Diffraction (XRD), Scanning Electron Microscopy (SEM), Energy Dispersive X-ray Spectroscopy (EDS) Transmission Electron Microscopy (TEM), Atomic Force Microscopy (AFM), Optical Profilometer (OP), and X-ray Photoelectron Spectroscopy (XPS) in order to see the surface and bulk characteristics.

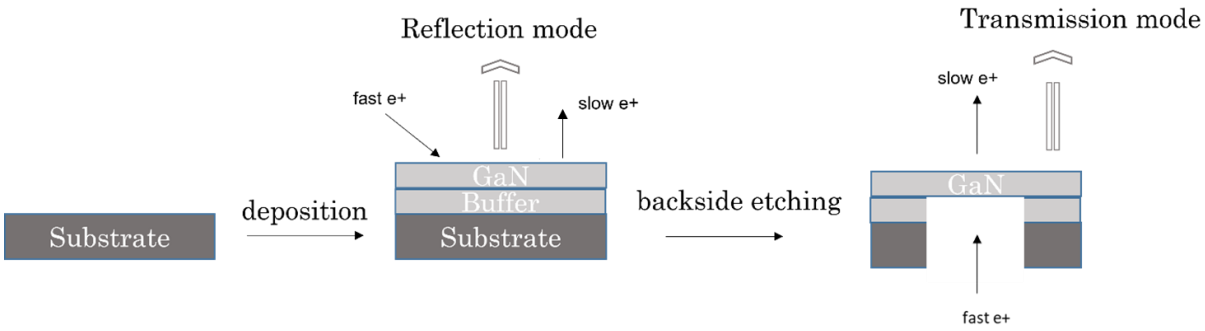

Figure 3.1 Step-by-step diagram showing the fabrication of the positron moderator based on GaN film

3.1 Experimental setup

The ELI-NP Targets Laboratory UHV (ultra-high vacuum) deposition cluster was used to grow thin films. It has three main vacuum chambers: i) the loadlock chamber in which physical etching with Ar ions can be done; ii) the sputtering chamber dedicated to metals and; iii) the chamber dedicated to oxides.

Before the experiment, some aspects require exhaustively research in the literature. Besides the sputtering target characteristics and the proper substrate material, there are other specific equipment parameters such as the operating regime (DC/RF), target-substrate distance, magnetron tilt, gas atmosphere, sputtering power, working pressure, substrate temperature, and rotation that should be adapted to the desired experiment.

The vacuum profile of the UHV chamber was the first important factor monitored during each deposition. The thicknesses of the deposited films were assessed using QCM, and it was calibrated by measuring the resulting film thickness with X-ray reflectivity (XRR). The actual temperature of the substrate and its behavior during deposition was studied. Additionally, plasma and target parameters were monitored. Direct current voltage (DCV) monitors the stability of the plasma profile and it is used for power regulation feedback for the RF unit. Variations in target surface resistance are often indicated by the reflected power.

This study does not cover the unsuccessful trials or equipment failures, atmospheric contamination, interrupted depositions, repetitions, deposition sets with small changes, setup difficulties resulting in vacuum loss, *etc*.

3.2 A short introduction to the characterization methods.

Further, the resulting samples were analyzed at the surface as well as in the bulk. XRD was used to characterize the microstructure of the samples. The fundamental idea behind this method is founded on Bragg's law of diffraction $n\lambda = 2d_{hkl}\sin\theta$, where n is an integer, d_{hkl} is the distance between atomic planes, λ is the X-ray wavelength and θ is the diffraction angle. When a collimated X-ray beam is incident on a crystal, the X-rays interact with the atoms in the crystal lattice and are scattered in various directions There is no evidence of diffraction peaks until the criterion for constructive interference is met, $\delta = n\lambda$ [53]. A Rigaku SmartLab diffractometer was used, characterized by a four-circle goniometer with an in-plane arm, a 9 kW rotating anode, a hybrid multi-dimensional (0D, 1D, 2D) pixel HyPix 3000 detector, 0.4 mm^2 microfocus area, SAXS (Small-Angle X-ray Scattering), and USAXS (Ultra Small-Angle X-ray Scattering) options, Ge (220) monochromators on the incidence and receiving optics.

SEM, along with Energy Dispersive X-ray (EDS), and Electron Backscatter Diffraction (EBSD) can be used to determine the chemical composition, texture (external morphology), crystalline structure, and material orientation of sample compounds. The SEM technique operates on the idea of hitting a sample with a focused electron beam and then analyzing the deflected electrons collected by a detector. As shown in Figure 3.2 (reflected part), when an electron beam hits a thick probe three types of electrons (SE-secondary electrons, Auger electrons, and BSE-backscatter electrons), X-rays, and cathodoluminescence are produced. For imaging of the samples, backscatter electrons and secondary electrons are used, i.e., BSE demonstrates the compositional difference in multiphase samples while SE reveals

the topography and morphology of materials. In reality, the picture is a distribution map of the signal intensity emitted by the scanned region [54].

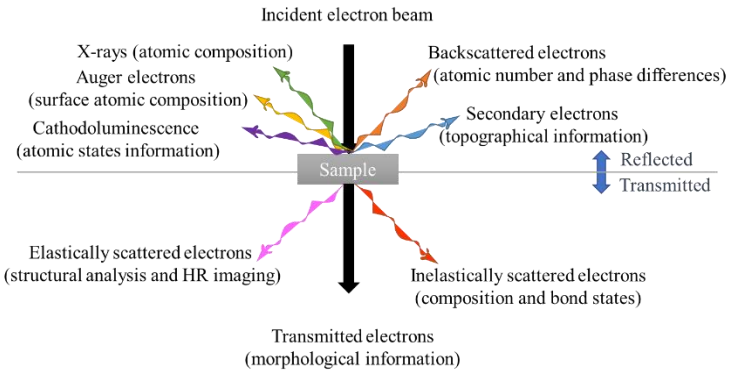

Figure 3.2 Summary of various signals obtained by electron interaction with matter

The measurements were performed using a High-resolution SEM (HR-SEM) Tescan MAIA-3. Elemental and chemical analysis, mapping, and line scans of the samples were performed by means of the EDS integrated into the HR-SEM chamber. In addition, TEM provides information about the arrangement of atoms in the sample and defects in the crystalline structure. Compared with the SEM technique which collects the deflected electrons that hit the sample, TEM reveals information after the electrons are transmitted through a thin sample, as shown in Figure 3.2. The crystalline structure of the samples was analyzed using a Cs-corrected Titan Themis 200 microscope (Thermo Fisher Scientific, Waltham, MA, USA) designed with a high-brightness electron source. Elemental line profiling was performed using a STEM detector and a Super-X EDS detector for Selected Area Electron Diffraction (SAED). EDS data processing was performed using ImageJ software [55], while SingleCrystal® (Oxford, UK) and CrystalMaker® (Oxford, UK) were used for simulating the SAED data and crystal structures [56].

In addition, topographic investigations were done by using AFM and OP (optical profilometry). There are three modes of measurement available on the AFM. (i) Contact or static mode: The probe is in proximity to the sample surface and does not oscillate; (ii) A mode in which the probe is not in touch with the sample (non-contact or dynamic mode). The probe oscillates over the surface of the sample without making contact with the surface; and (iii) Tapping, semi-contact or intermittent contact mode: At the bottom of the probe's oscillation, the tip comes into close contact with the surface of the sample [57]. In contrast, optical

profilometry exploits light rather than a physical probe. This may be accomplished in several ways. The key to this technique is redirecting the light such that it can detect the surface in three dimensions. Examples include optical interference, confocal aperture use, focus and phase detection, and the projection of a pattern onto an optical picture [58]. In semi-contact AFM images were recorded by the NTEGRA scanning probe microscope, while the surface profiling characterization with 3D images and 2D profiles was collected using the interferometric method by the specific DI 50× objective of the Optical profilometer SENSOFAR S-neox.

Electronic Structure for Chemical Analysis (ESCA), or XPS is the method used in this research for determining the chemical composition of the sample surfaces (from 1 to 5 nm). A constant energy X-ray radiation (in practice, one uses excitation radiation K_α emitted by the anode of Al with 1486.7 eV or Mg with 1253.6 eV) excites electrons from the shells of the sample's constituent atoms, which are then emitted as free electrons with kinetic energy (*KE*) equal to the difference between excitation radiation energy (*hv*), binding energy (*BE*), and the work function of the electrons from the material [59]. The diagram of the photoelectric effect in XPS is presented in Figure 3.3. The measured *KE* provides the elemental analysis due to the specific BE for a given charge number. Sigma Surface Science photoelectron spectrometer was used to record XPS spectra. This equipment uses a 160-mm hemispherical energy analyzer with a 1D detector (ASPECT) and an Al K_α/Mg K_α X-ray source.

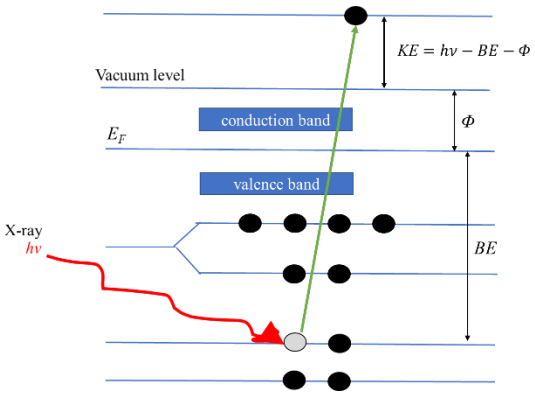

Figure 3.3 Diagram of photoelectric effect in XPS

3.3 Gallium nitride deposition

The targets that were used in this research are GaN commercially available targets. First polycrystalline target, noted further as $T_{GaN\text{-}Pa}$, was purchased from American Elements. The last two targets were bought from SurfaceNet GmbH, one as polycrystalline GaN, noted as $T_{GaN\text{-}Pb}$, and one monocrystalline GaN, noted as $T_{GaN\text{-}M}$. Before the sputtering procedure, each target used for GaN deposition was subjected to XRD and HR-SEM/EDS measurements in order to get a clear image of the crystal structure, preferred orientation, and chemical composition.

Using the ultra-high-vacuum (UHV) deposition cluster, GaN thin films were grown by radio frequency (RF) sputtering. Si, TiO_2, ZnO, and Al_2O_3 substrates were used for deposition. Before deposition, the substrates were cleaned as it was explained prior in this chapter. Further, they were fixed with silver paste on the sample holder, then heated at 100 ^oC for 20 minutes to evaporate the silver paste's solvent. To eliminate any residual impurities, samples were annealed for 1-2 hours at 300-550 °C under vacuum (~10^{-6} mbar). The parameters for GaN deposition include a working pressure (P_d) from 8×10^{-3} to 1.15×10^{-2} mbar, which is comprised of a mixture of argon and nitrogen in the plasma volume. The temperature of the substrate was set from 450 ^oC to 700 ^oC, and its distance (d_{ts}) from the target was set to 10-20 centimeters. The magnetron operated at a power (P_s) of 50 to100 watts, and a presputtering procedure, which aimed to clean the target, was carried out for 30 minutes while the shutter in front of the substrate was closed. In addition to this, the GaN target was RF sputtered with for a period (t) between 30 and 90 minutes. After the deposition was complete, the sample heating was switched off, and the sample was allowed to return to ambient temperature while still contained inside the deposition chamber.

The X-ray reflectivity (XRR) was applied to evaluate numerous characteristics of the films, such as the layered structure, the density, information on the thickness of the interfaces, and the film thickness, which was also used for QCM calibration.

The ex-situ AFM characterization, which was performed in the semi-contact mode, showed the growth mode. This growth type is characterized by 2D-islands growth for R1/Al_2O_3, R2/Al_2O_3, and R4/ZnO, and transition to a 3D growth for R3/Al_2O_3, R5/ZnO, and R6/TiO_2. AFM images of thin and thick GaN films produced on an Al_2O_3 substrate are shown in Figure 3.4.

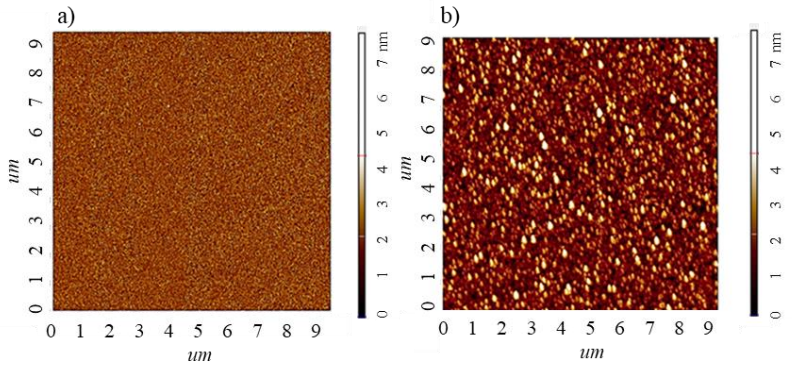

Figure 3.4 AFM images of the GaN films with different thickness growth on Al_2O_3 substrate (a) thin film, (b) thick film

SEM-EDS investigations were needed to assess the clear view of the surface morphology and the qualitative elemental composition of the films. The SEM examination revealed smooth, uniform, crack-free surfaces with a homogenous morphology at a few micrometers scale.

For a more accurate surface analysis XPS measurements, in the binding energy range of 0-1200 eV were done. The ratio obtained was approximately Ga_1 N_3 O_2 for all the $T_{GaN\text{-}Pa}$ samples. This behaviour was assigned to the cooling down of the samples in the nitrogen atmosphere from the deposition temperature to the room temperature which result in surface nitridation. The assumption is sustained also by the EDS measurements of GaN films which show contradictory Ga:N ratios with XPS results. Ga:N ratio obtained for the $T_{GaN\text{-}Pb}$ samples was approx. Ga_1 $N_{0.9}$, while $T_{GaN\text{-}M}$ samples present approx. 1:1 Ga:N ratio. As well as, the EDS results reflect these ratios for the GaN films obtained with $T_{GaN\text{-}Pb}$ and $T_{GaN\text{-}M}$ targets.

Moreover, some of the samples have been structurally investigated by TEM. The interface presents defects such as linear dislocation and point defects. At the surface of the substrate, the samples manifest a disordered microstructure that results in a high density of dislocation defects found inside the polycrystalline film.

In summary, the as-deposited films correlate with the chemical composition of the GaN targets. Different deposition parameters were implied in the attempt of getting a defect-free GaN film. Unstable, sporadic glow discharge was observed when the used Ar:N_2 ratio was 10% Ar - 90% N_2 and 40% Ar - 60% N_2. It was discovered that an atmosphere with a composition of 70% N_2 and 30% Ar would have an approximate Ga:N ratio of 1:1 and significantly lower oxygen content.

3.4 Buffer layer

Literature reviews reveal that a buffer layer is needed between the substrate and the GaN film to assist the film's relaxation from stress and strain that might occur during film growth caused by lattice mismatch [60], [61].

3.4.1 Aluminum nitride (AlN)

Fallowing the same cleaning procedure as that was used for GaN films deposition, efforts are made to create an AlN buffer layer using a 1- inch Al target. These attempts were undertaken on Si (111) substrates. In Figure 3.5 are presented the 2-theta scans of samples SA1 (purple), SA2 (yellow), SA3 (orange), SA4 (dark green), SA5 (blue), SA6 (light green), a spectrum belonging to the untreated Si(111) substrate (grey), and a Si(111) substrate treated at 700oC (black - monochromator measurement). In these spectra no peaks belonging to AlN could be observed, instead, the (222) reflection of the silicon substrate could be observed. The peaks ~42^o are attributed to the signal that came from the Al sample holder.

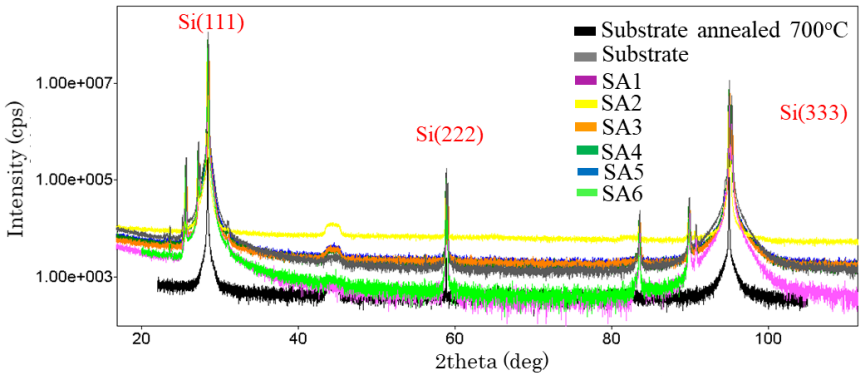

Figure 3.5. XRD 2theta scans for the AlN layers grown on Si substrates

3.4.2 Zinc oxide (ZnO)

Efforts are being made to create a ZnO buffer layer by using a ZnO target that is 1 inch in diameter. All of the samples were successful in producing the zinc oxide layer, as seen by the 2-theta scans displayed in Figure 3.6.

Copper contamination was found in both of the most recent depositions. This feature arises as a result of a bad electric contact that melted the copper that is located at the back of the target (back-side Cu plate) and evaporated it at the same time as the zinc oxide. As a direct consequence of this, depositions were halted once the target was compromised.

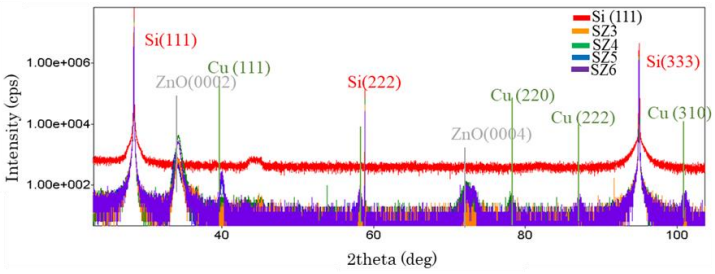

Figure 3.6 XRD 2theta scans for the ZnO layers grown on Si substrates

3.4.3 Titanium nitride (TiN)

In the vacuum environment, achievements have been made in producing TiN buffer layers by using a titanium target and an atmosphere that consists of both argon and nitrogen. These two gases have been used in different ratios to create the proper gas mixture to grow TiN layers. The Si(111) substrates were placed into the deposition chamber after undergoing the identical cleaning and bonding steps on the sample holder as indicated in the previous studies.

As an example, Figure 3.7 show the XRD results for ST4. The TiN phase identified in the sample has a (200) orientation. Moreover, it was discovered that the values that were used for ST4 are the optimal deposition parameters.

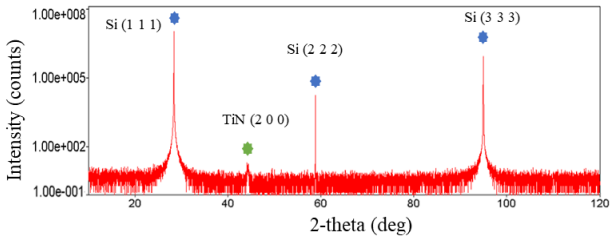

Figure 3.7 XRD 2theta scan of ST4 showing TiN (200)

3.5 Summary

The goal of this research was to create a novel transmission or reflection mode moderator or a field-assisted moderator. XRD and HR-SEM/EDS were used to characterize the microstructure and crystallographic orientation of the samples, while SEM and EDS were used to determine elemental composition, texture, and crystalline structure of the sample compounds. XPS was used to determine the chemical composition of the sample surfaces. Thickness ratios and preferred orientations of GaN and GaN/Ga_2O_3 were determined by the substrate's spatial group. AlN buffer was impossible to achieved due to a highly oxidized Al target. ZnO buffer was obtained, but cooper contamination was found in latest films. TiN phase with (200) orientation was obtained by using a Ti target.

Based on part of these results, a paper was written and published in the Scientific Bulletin of the University Politehnica of Bucharest [62]. The publishing of the study was the result of a joint effort by the group Department of Science and Engineering of Oxide Materials and Nanomaterials, UPB, and Target Laboratory group, ELI-NP.

Chapter 4

Studies on commercially available GaN samples

Besides being a perspective material for positron moderation [63], [64], gallium nitride is an important wide band-gap semiconductor also used in the fabrication of nitride based heterostructure devices for photodetectors [65], electronics [66], [67], light emitting diodes [68], [69]. In this sense, understanding GaN's defect structure becomes vital since any impurities, vacancy defects, or strains can influence its unique physical and optical characteristics [66], [70], [71].

4.1 Materials and Methods

In the present chapter, a report of the analysis of the crystal quality of a commercially available GaN epitaxial thin film grown on (111) 3C-SiC with an intermediate AlN buffer layer is presented, along with an analogy with other GaN samples grown on Si (111) and Al_2O_3 (0001) substrates. The samples used in this

chapter were produced at NTT Advanced Technology Corporation (Kanagawa, Japan) for high-electron-mobility transistors. As it was presented in Ref. [72], [73], the films' exact growth conditions were not made available by the producer. Complementary techniques were applied for characterization of the material in order to study the microstructure, interfaces' characteristics, and defects distribution. The samples were investigated via HR-TEM, HR-XRD, SEM-EDS and DBS.

4.2 Results and Discussion

Concerning determining the sample structure of the GaN layers, out-of-plane 2theta-omega scans were undertaken. GaN was confirmed to be a single-phase hexagonal structure, orientated along the c-axis, and present in all of the samples, i.e., Si, Al_2O_3, and SiC substrates. In the out-of-plane 2theta-omega scans, the (000l) reflections of the hexagonal AlN (ICDD 00-025-1133) were also observed. The omega scans of the (000*l*) (*l* = 2,4) reveal that the sample with the highest quality (smaller amount of defects) is GaN/SiC, while the sample with the lowest quality (bigger amount of defects) is GaN/Al_2O_3, which exhibits an FWHM of 0.234°.

The SEM micrographs of GaN300/Si presents a surface with holes, while GaN/SiC has a smooth surface. In the GaN/ Al_2O_3 micrograph was noticed the hexagonal shape of the GaN, which is measured on the edge of the sample. The evaluation of the TEM cross-section images confirmed the buffer layer of aluminum nitride (AlN), therefore, the GaN/SiC sample can be regarded as a GaN/AlN/SiC heterostructure. Usually, such a layer aims at reducing the number of defects in the GaN film on account of the low lattice mismatch between AlN and GaN of 2.4% [74].

For the assessment of the threading dislocation density, ρ_{d}, and the correlation length, *L*, several double-axis ω scans (rocking curves) were performed for selected (*h k l*) planes. The obtained threading dislocation densities corresponding to the GaN layer grown on SiC are $\rho_{\mathrm{d}}^{\mathrm{e}}$= 1.37×10^{10} cm^{-2} and $\rho_{\mathrm{d}}^{\mathrm{s}}$ = 1.07×10^{9} cm^{-2}. Consequently, the total threading dislocation density calculated as the sum of those two component densities is $\rho_{\mathrm{d}}^{\mathrm{t}}$ = 1.47×10^{10} cm^{-2}. With the later value, the mean distance between two dislocations was determined as being 82 nm according to $r_d = 1/(\rho_{\mathrm{d}}^{\mathrm{t}})^{1/2}$ [75].

The values of the dislocation correlation lengths, *i.e.*, L^e= 171 nm and L^s = 288 nm, extracted from the peak profiles, can be ascribed to the low lattice mismatch between the substrate and the film. The uncertainty of the presented values is within the least significant digit.

According to Figure 4.1, a strong decrease in S was observed for $E_+ \lesssim 1$ keV due to the reduced ability of thermalized positrons to diffuse back toward the surface. This phenomenon is induced by the local electric field resulting from the band bending near the surface. Consequently, less Ps emission takes place at the surface and thus the positron diffusion length is reduced. At $E_+ \gtrsim 1$ keV, S increases slowly with E_+ in the GaN film area, then seemingly reaches a plateau in the AlN layer (for $E_+ \gtrsim 17$ keV), before finally achieving full saturation at $E_+ \gtrsim 21$ keV within the SiC substrate layer.

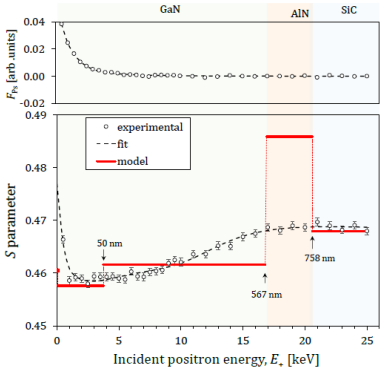

Figure 4.1 Plotted depth profiles $S(E_+)$ of GaN/SiC. The experimental errors are in the order of the experimental point size. The stairs represent the best parameters obtained by the fit of a 4-layer model to the experimental data by the VEPFIT software. The values represent the cumulative thickness of the layers. The upper part of figure is the experimental data and the best fit of the relative Ps fraction, $F_{Ps}(E_+)$

Since Ps is not formed within the bulk GaN layers, the inequality S_{GaN1} = 0.4576 ± 0.0004 < S_{GaN2} = 0.4615 ± 0.0004 indicates either smaller (in size) or a lesser number of defects, as well as a longer L_{eff} within the GaN1 sublayer [76]. Given the resulting disagreement in L_{eff}^{GaN1} = 13 ± 0.4 nm being smaller than L_{eff}^{GaN2} = 75 ± 20 nm the underlying reason could be related to the presence of a local electric field directed toward the surface.

The results which summarize the characteristics of the GaN layers, listed in this study along with previously reported results [72], [73] are shown in Table 4.1.

Comparing the results, one can observe that GaN exhibits an improved crystal quality in the sample GaN/SiC, with the lowest structural defect density ρ_d^t = 1.47 × 10^{10} cm^{-2}, the highest value of L_{eff}^{GaN2} = 78 ± 20 nm, and the narrowest omega scans.

Table 4.1. Total defect densities, defect correlation lengths and effective positron diffusion lengths in GaN, where *d* is the layer thickness, ρ_d^t is the total threading dislocation density, r_d is the mean distance between two dislocations, *L* is the defect correlation length (edge and screw) and L_{eff} is the effective positron diffusion length

Sample	d_{GaN} [nm]	ρ_d^t [cm^{-2}]	r_d [nm]	*L* [nm]		L_{eff} [nm]	
				L^e	L^s	GaN1	GaN2
GaN/Al_2O_3 [72]	189	7.49× 10^{10}	36	155	229	12.4 ± 0.4	56 ± 4
GaN300/Si [73]	350	4.37 × 10^{11}	15	27	107	14.3 ± 0.5	22 ± 6
GaN700/Si [73]	690	2.35 × 10^{11}	21	41	220	13.1 ± 0.4	43 ± 6
GaN/SiC	567	1.47× 10^{10}	82	171	288	13.0 ± 0.4	78 ± 20

4.3 Summary

The relationship between the substrate-buffer-film heterostructure and the consistency of its interfaces, layer thicknesses, dislocation densities, and positron-characteristic diffusion lengths in the GaN/AlN/SiC heterostructure was evaluated using a several methods.

This research was completed with the contribution of V.L. Ene and B.S. Vasile (University Politehnica of Bucharest) for the TEM measurements and analysis, I. Zai and V. Leca for the threading dislocation densities measurements and analysis (ELI-NP) and D. Dinescu and N. Djourelov (ELI-NP) for the positron investigation of the GaN films. Based on these results, three articles were published, two in Nanomaterials (Basel) [73], [77] and one in Materials (Basel) [72]. This thesis presents only the results from the publication authored by A.B. Serban *et.al.* “Studies of Defect Structure in Epitaxial AlN/GaN Films Grown on (111) 3C- SiC” [77]. This article is a comprehensive analysis of the experimental results obtained on all three GaN samples.

Chapter 5

Optimization and manufacture of the positron moderation device based on a magnetic bottle

Accelerators, ultra-intense short pulsed lasers, and nuclear reactors are used to produce positrons. The energy spectrum of positrons emitted from source ranges from keV to few MeV. To study subsurface regions, thin films, or layered structures, the positron energy bandwidth must be narrowed down to a few eV. The best known way is a two-step process involving positron moderation. The first step is energetic, fast positrons to be converted to a beam of slow positrons and, then as a second step, to be accelerated to a controllable energy. Single-crystalline tungsten foils and tungsten meshes are the best work function moderators [78], [79], and frozen rare gases are the effective moderators that take use of the extended diffusive length [80].

According to the results of Gerchow *et al.* [18], the magnetic bottle trap may enhance the positron moderation efficiency of a tungsten foil by a factor of 20. This device is made up of a vacuum chamber and two coils, which generate an axisymmetric saddle-type magnetic field to trap fast positrons emitted from a ^{48}V

foil. It is low cost and ease of operation, and can be used in the ELIPS experimental setup. Additionally, a cyclotron is available at the "Horia Hulubei" National R&D Institute of Physics and Nuclear Engineering (IFIN- HH) [81] and the TR19 team already has expertise to produce the ^{48}V radioisotope [82]. This method increases the quantity of positrons accessible for the moderation process, which ultimately results in a better level of efficiency.

5.1 The magnetic bottle device concept.

Positron confinement in a mirror machine was first described in 1960 by Gibson *et al* [83]. Simons suggested using a magnetic bottle with a thin foil positioned in the center as an energy degrader in the 1980s [84], [85]. Waeber *et al*. [86] attempted to use the same strategy to reduce the energy of positrons to a few keV prior to extracting them and moderating them outside the magnetic bottle to create a mono-energetic beam. Gerchow *et al*. [18] recently described a positron moderation device based on a magnetic bottle trap, also known as a magnetic mirror machine, which traps the majority of the positrons emitted from a 1-μm-thick ^{48}V foil made from a Ti foil activated by 12-MeV proton irradiation. The magnetic field has a maximum value at the center of each coil and a local minimum between the coils leading to a confinement of charged particles. The particles move along spiral paths aligned with the axis of the trap as they go between the two coils.

5.1.1 Ideal positron magnetic bottle

The schematic of the magnetic bottle device is shown in Figure 5.1. It consists of two magnetic mirrors. The maximum gyromagnetic radius, r_g, of the released positrons is multiplied to estimate the minimum radial dimension of the vacuum chamber in an ideal magnetic bottle.

The greatest r_g could well be evaluated using the positron's mass, m_e, the endpoint energy of emitted positrons, E_b (E_b = 694.68 eV for ^{48}V), the electron charge, q, and $B_z^{ave}(z=0) = \int_{x=0}^{r_{ch}} B_z(z=0,x)\mathrm{d}x$ (r_{ch} denotes the chamber radius), as:

$$r_g = (2m_e E_b)^{0.5}/(qB_z^{ave}(z = 0)) \quad . \quad 5.1$$

The pitch-angle, Θ, is what determines the loss cone, and the equation that describes it is as follows:

$$\Theta = (R_m - 1)^{-0.5} \quad 5.2$$

with $R_m = B^{max}/B^{min}$ being the mirror ratio and B_z^{max} denoting the $B_z(z, r = 0)$ maximum, and B_z^{min} denoting the local minimum $B_z(z = 0, r = 0)$.

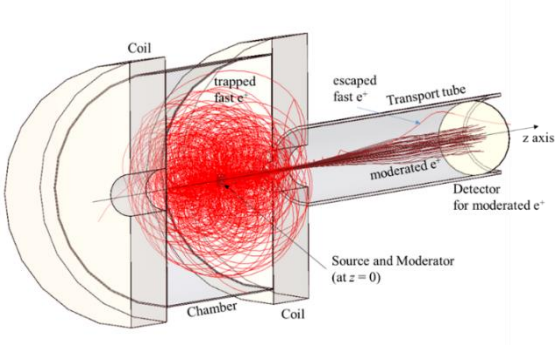

Figure 5.1 Sectional diagram of the magnetic bottle device showing a chamber with two coils functioning as magnetic mirrors and a transport tube [87]

To be trapped, positrons need to have a velocity component ratio of $v_z/v_r \leq \tan \Theta$. An ideal two-coil trap would contain enormous coils of radius ~$2r_g$ delivering high B_{max} simultaneously, with the coils spaced such that $B_z(z = 0, r)$ satisfies eq. 5.1. Consequently, the construction of a powerful and, at the same time, huge magnetic coil is quite costly, and the optimization technique should take into account specific geometrical and budgetary elements.

5.1.2 Design limitations. Fast positron source and moderator

High-temperature superconducting strips are an excellent conductor for creating a strong magnetic field, but they are expensive and require a lot of expertise and guesswork. A commercial copper conductor with a cross-section of 12.5×8.5 mm^2 and a hollow channel of diameter ø4.3 mm is suitable for building the coils when excited by a 10 kW power supply. The maximum allowable current is bounded by the specific resistivity of copper and the total conductor length. Parameters of feasible coil layouts are listed in Table 5.1.

Table 5.1 Outer radius, coil thickness, windings per coil, maximum current, and total conductor length are calculated. The additional insulation surrounding the conductors is included (0.5 mm) in the coil's diameter and thickness. Maximum coil current must be lower than the power supply's maximum current [87]

Configuration / Parameter	L8w10	L9w9	L9w8	L10w7	L11w6	L12w5	L14w4	L16w3	L20w2
Radial layers	8	9	9	10	11	12	14	16	20
Windings per layer	10	9	8	7	6	5	4	3	2
Outer radius, r_{co} (mm)	94.5	104.0	104.0	113.5	123.0	132.5	151.5	170.5	208.5
Coil thickness (mm)	130.5	117.5	104.5	91.5	78.5	65.5	52.5	39.5	26.5
Maximum current (A)	1000	917	1000	985	975	1000	958	1000	1000
Conductor length (m) for two coils	54.3	59.6	53.0	55.4	56.0	54.3	57.0	54.3	54.3

In order to prevent the loss of trapped positrons as a result of interaction inside the chamber volume, the positron source foil, the moderator and mesh's support structure must be constructed using as little material as is humanly feasible.

5.2 Numerical simulations procedure

Dryzek and Horodek presented evidence that GEANT4 algorithms produce implantation patterns that are consistent with the results of experiments [88]. A user-physics technique was developed for selecting the positrons that would be moderated based on their interaction with the moderator material, and then compelled the positrons to be pumped into the vacuum in their moderated state. The probability of a thermalized positron diffusing to the surface is computed using the distance d to the closest surface and the e^+ diffusion length i.e. $p = \exp(-d/L_+)$. Both the W foil moderator and fast e^+ sources for transmission and backscattering mode, respectively, were established according to their respective descriptions in references [18] and [89].

COMSOL [90] is used to calculate the magnetic and electric fields present in the magnetic bottle device, and the 3D files of the device's geometry are compared to those from GEANT4 to validate the simulation approach. There is no information provided by the authors on the geometrical dimensions of the magnetic bottle. The magnetic field with values of $B_{max} = 2559$ G and $B_{min} = 544$ G, and 66% of the positrons mirrored from the ^{48}V source moderation efficiency was achieved using a configuration of two coils with an inner radius of 78 mm, an outer radius of 200 mm,

a thickness of 50 mm, and each providing magnetomotive force of 53300 ampere- turn. The extraction efficiency was 94%. An electric field between the grounded chamber and the moderator-source assembly at a higher potential of 600 V guaranteed a hundred percent extraction rate. Our model estimated $\varepsilon_{\#1}$ = (0.24 ± 0.02) %. The fact that the branching ratio value Y_0 = 0.33 was neglected in the Gerchow *et al*. [18] experiment might be the reason for the large variation between the two results. Slow positron beamlines with magnetic guidance use a series of coils or long solenoids with an axial magnetic flux density, B_z^t, of around 100 G. As seen in Figure 5.1, the current arrangement includes a lengthy solenoid.

5.3 Numerical simulations results

Moderated positrons drift down the z-axis with a small gyromagnetic radius, and the B_z has an inverse relationship with the cross-section profile of the resulting slow positron beam. A simulated spot of moderated positrons within the solenoid for magnetic guidance B_z^t = 100 G is shown in Figure 5.2. The primary objective was to examine coil configuration from setup #1 in relation to coil configurations that would work with a 10 kW power source.

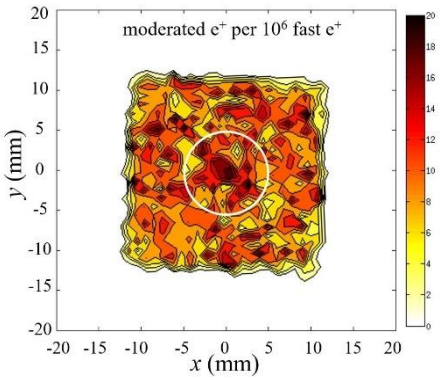

Figure 5.2 Moderated positrons spot for the coils' configuration L10w7 under magnetic guiding B_z^t = 100 G inside the transport solenoid. The white circle marks the central ∅10 mm area [87]

The simulated B_{min} is set to be equal to 544 G as in setup #1, by the adjustment of the length, h_{ch}, of the chamber. So that a comparable amount of positrons may reach and annihilate the cylindrical wall of the chamber in each of

the listed coils' configurations. To illustrate this, Figure 5.3 displays the calculated (total and "useful" moderated positrons) value of B_{max} as well as the proportion of 10^6 released fast positrons that are detected as moderated positrons in the transport tube.

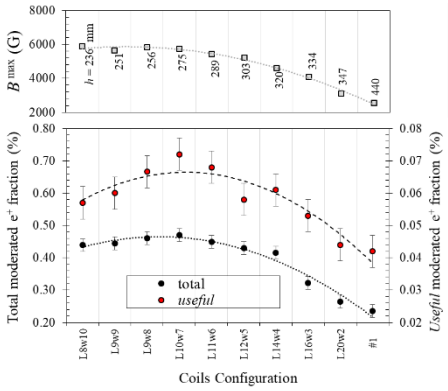

Figure 5.3 Fraction of the total and "useful" detected moderated positrons together with B_{max} in the case of coils' configuration presented in Table 5.1 [87]

The chamber length of h_{ch} =300mm is a reasonable compromise for achieving total and useful moderated e^+ percentages near to their maximum values. The chamber with $r_{ch} = 100$ mm will be chosen the most suited for the implementation of the device because of the lower cost for lead shield protection. The depth profiles of the simulated positrons that are emitted from the 1-μm-thick ^{48}V foil and implanted in the 1-μm-thick W moderator foil before they are annihilated are shown in Figure 5.4. This study compared the effect of setup #1 and the optimized setup on the moderation efficiency of positrons stopped in the layer between 0.9-1 μm of the moderator. The results showed that the optimized setup had nearly twice as much moderation efficiency as setup #1.

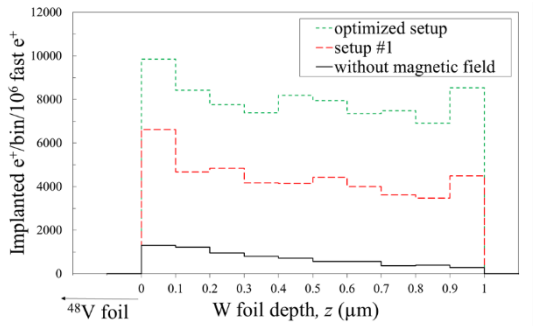

Figure 5.4 Simulated z-axis position of positrons from 1-μm-thick ^{48}V implanted in 1-μm-thick W [87]

The overall moderated e^+ proportion is calculated from the particular activity data, and from that, the initial slow e^+ intensity for 8-h-activation of the source foil as a function of thickness is estimated in Figure 5.5. To get a stronger ^{48}V at a set time for proton irradiation and within the limitation of the proton beam cross-section profile, increase the thickness of the Ti foil.

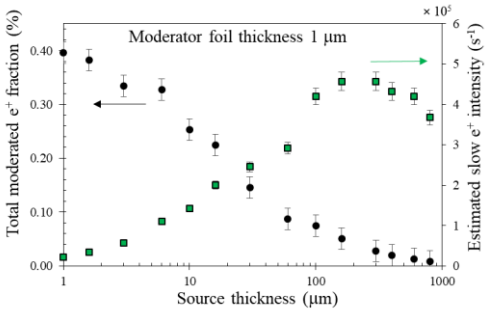

Figure 5.5 Simulated total moderated e^+ fraction and estimated initial slow e^+ intensity for 8-h-activation of the source foil as a function of thickness of the source foil [87]

The simulation results of the overall fraction of moderated e^+ as a function of the thickness of the moderation W foil for source foils of thickness 1 and 10 µm are shown in Figure 5.6. Results show that for a given moderator thickness, the desirable value is somewhere between 1 ÷ 2 µm.

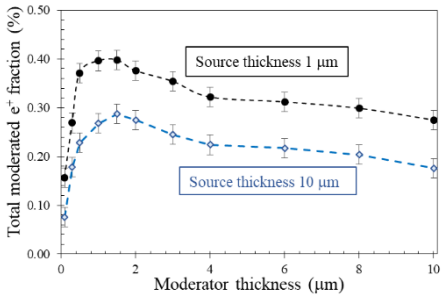

Figure 5.6 Simulated total moderated e^+ fraction as a function of thickness of the moderation foil in cases of source foil thickness 1 and 10 µm [87]

5.4 Manufacturing of the positron moderation device

5.4.1 Magnetic coils construction

The National Institute of Research & Development in Electrical Engineering – Bucharest (ICPE-CA) was specifically involved in the manufacturing of the magnetic coils. Electromagnetic coils were settled upon for construction using standard hollowed copper conductor in the dimensions derived from the aforementioned optimization research (see Table 5.1.). High-purity (99.97%), hollowed copper conductor was chosen; it was insulated with glass fiber and resin. Vacuum was used to embed the coils in epoxy resin (without air bubbles).

5.5 Designing and assembling the experimental setup

In order for the magnetic bottle chamber to be made, a three-dimensional design has been prepared for it, along with drawings that can be used in production. Stainless steel was used for the construction of all of the flanges, tubes, and side walls. In preparation for the application of a vacuum of 10^{-7} mbar, the chamber was cleaned, conditioned, and subjected to helium leak testing. In addition to that, a water-cooling system was implemented up in the experimental hall specifically for the coils. Further, the magnets and the cables were assembled together with the vacuum chamber and were connected to the water cooling system as can be seen in the Figure 5.7.

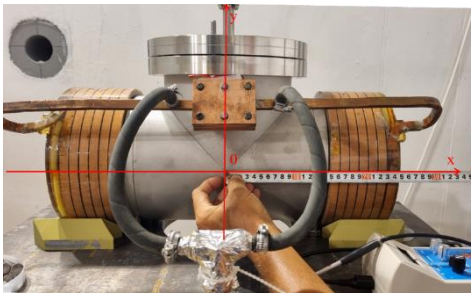

Figure 5.7 Vacuum chamber and magnets assembled together. Magnetic field measuring axes

In order to determine the level of heat generated by the magnets, tests of the water cooling circuit were carried out. The magnet reaches a temperature of 57 ^{o}C when

subjected to the highest current that may be applied. This temperature limits the power supply to a current of less than 928 A, which results in an applied power of less than 9.7 kW. The in-vacuum supporting structure was conceived of and built in such a manner that any potential losses of trapped positrons arising from contact inside the chamber volume were eliminated throughout the production process. To be more specific, the support of the positron source foils, the moderator foil, and the mesh were all designed to use the minimum amount of material feasible.

Finally, the experimental setup was assembled, including the positron transport tube, the analysis cross, the detectors, the vacuum pumps, and all of the associated power supplies. The experimental ensemble is presented in Figure 5.8.

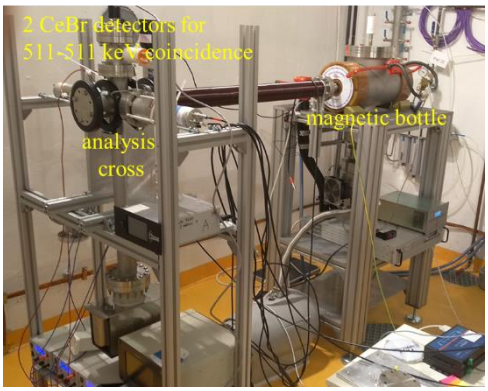

Figure 5.8 Magnetic bottle experimental setup with analysis cross equipped with two $CeBr_3$detectors.

5.5.1 Ti foils irradiation

The irradiation of 4 foils with dimension of 10×10mm^2, thickness of 2 μm each, and purity of 99.6% was performed by stacking them in the irradiation holder. The extracted proton energy was E_{extr} = 14 MeV and the proton beam energy at the titanium target was E_{inc} = 13.2 MeV. The irradiation time was 1 h.The proton current had a value of I_p = 5 μA. The integral current of 5.0 μAh yielded an activity of ^{48}V of A_{EoB} = 245.5 kBq per foil and $A_{EoB\ (4\ foils)}$= 982 kBq for 4 foils.

5.5.2 W annealing

An annealing temperature of approximately 2600 ºC, which is equivalent to 0.7 T_M (melting temperature of W in Kelvin), is desirable [91] in order to remove any

imperfections that may have been still in the tungsten material. This is because tungsten has a high melting point, which is 3422 ºC. In addition, an annealing temperature of roughly 1500 ºC is necessary [92] in order to purge the material of any surface contaminations, such as oxides. A chamber that will be used for the annealing of the tungsten foil (moderator) via the use of electron bombardment has been developed and constructed. W foil annealing, was performed in a vacuum level below 5×10^{-6} mbar. The temperature measured by the pyrometer was ~ 2050 ºC and was kept in 2 complete cycles in which the electron beam covers the entire foil.

5.6 Results

The first step towards understanding what to expect from the experimental results was to simulate the physics processes for the optimized setup with the real dimensions and conditions. It was demonstrated that all moderated and some fast positrons are escaping from the bottle and transported through the transport tube to the analysis cross.

The data acquisition system is designed to measure the annihilation gamma rays of 511 keV energy emitted in opposite directions by detection by two ø3" × 3" $CeBr_3$ detectors placed transversaly to the positron beam axis outside the analysis cross. The experiment was performed with the W mesh (grid) kept at ground (0 potential). The W annealed moderator and the irradiated Ti foils were placed on the frame and introduced in the vacuum chamber (see Figure 5.9). The experiment was running at a given potential +200 V (*pushing* mode) and -200 V (*stopping* mode) applied on the W - ^{48}V foils. The +200 V potential was used as *pushing* mode for the moderated positrons to be pulled towards the transport line. The -200 V was used as *stopping* mode for blocking the moderated positrons.

A ø30 mm target was used in the analysis cross and a -1000 V potential was applied to accelerate the positrons that reach the target in order to be implanted and annihilate at some depth. The annihilation gamma rays of 511 keV energy emitted in opposite directions were detected by the two ø3"× 3" $CeBr_3$ detectors placed transversely to the positron beam direction. The acquisition electronics was set to work in coincidences, as in the calibration measurements, in order to eliminate gamma rays

that may appear from the annihilation of positrons on the walls of the chamber or transport tube. Each measurement lasted at least 1 h, and the estimated error in determination of the count rate of the coincidences was 4.6% of the measured value.

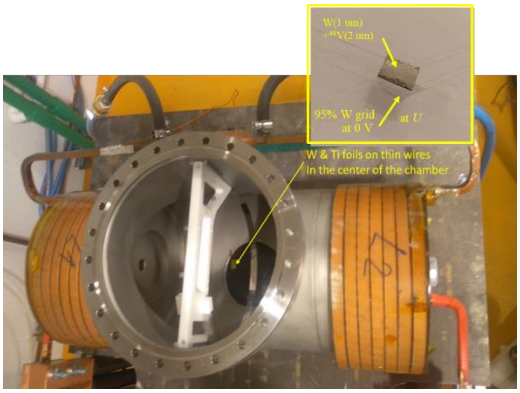

Figure 5.9 Magnetic bottle chamber assembled together with the frame

Further, the two modes *pushing* and *stopping* of the moderated positrons were measured. The difference between the *pushing* and *stopping* count rates represent the moderated positrons at the target. The ratio of this value to the count rate obtained when the corresponding ^{48}V foils were placed in the center of the analysis cross gives the moderation efficiency. In consequence, the comparison of the measured data with the simulated concerning the absolute values of the fast and moderated positrons at the target and the comparison of the measured and simulated data of the moderation efficiency as a function of the total thickness of the 48V foils demonstrated very good agreement.

5.7 Summary

The design optimization and manufacturing of a magnetic bottle device for high-efficiency positron moderation was described herein. The interaction between positrons and matter, including positron tracking, was performed via GEANT and COMSOL simulation. Stainless steel was used for the construction of all of the flanges, tubes, and side walls of the chamber. Irradiation of 4 foils with dimension of 10×10 mm^2, thickness of 2 μm each, and purity of 99.6% was performed by stacking them in the irradiation holder. A chamber that was used for the annealing of the tungsten foil (moderator) via the use of electron bombardment has been developed and constructed.

The W foil was annealed in a vacuum level below 5×10^{-6} mbar at a temperature ~ 2050 ºC and was kept in 2 complete cycles in which the electron beam covered the entire foil.

The comparison of the measured data with the simulated concerning the absolute values of the fast and moderated positrons at the target and the moderation efficiency as a function of the total thickness of the ^{48}V foils demonstrated very good agreement.

This research was a collaborative work between three groups: Positron Laboratory group, ELI-NP, Department of Non-Conventional Electrical Engineering, ICPE-CA, and Applied Nuclear Physics Department, IFIN-HH. The group from ICPE- CA was responsible for building the magnetic coils and the group from IFIN-HH for the Ti irradiation. Based on the optimization study, an article was published in Nuclear Inst. and Methods in Physics Research Section A, [87].

Chapter 6

Conclusions and perspectives

During the initial stage of this investigation, the primary focus was on developing a novel transmission or reflection mode moderator as well as a FA re-moderator. This first chapter describes the original study that was done to deposit GaN and its buffer layer, as well as the characterization of the films that were produced as a consequence in order to acquire a thin film material appropriate for positron moderation. A buffer layer was also considered as a potential approach to help the film relax from strain and stress. With an oxidized Al target, AlN buffer proved unable to accomplish. Although the ZnO buffer was formed on all of the samples, copper contamination was discovered, and as a result, depositions were halted once the target was damaged by a poor electrical contact. Using a Ti target, the TiN phase with (200) reflection was discovered in the deposited samples. It was shown that the attempts made to develop epitaxial films could not be successful under the circumstances described in the chapter.

To show that GaN is an appropriate positron moderator in the epitaxial ordered phase, the second chapter presents original research that analyzes the crystalline quality of commercially available GaN produced on three distinct substrates. The observed dislocation correlation lengths L^{e} = 171 nm and L^{s} =288

nm, and the mean distance between two dislocations (r_d = 82 nm) are greater than what was found in examined heterostructures on Si and Al_2O_3 substrates. This demonstrates that using AlN-SiC as a growth template for the GaN crystals results in a higher-grade crystal. In addition, the DBS measurements upheld the afore-mentioned results, with higher effective positron diffusion length $L_{\text{eff}}^{\text{GaN2}}$= 75 ± 20 nm for the GaN layer. It has been shown that the use of this material as a positron moderator is not appropriate given the proposed experimental setup.

A description of the original research that was undertaken with the aim of improving the performance of a magnetic bottle trap is discussed. The simulations demonstrated that the setup device with the adjusted parameters would have a moderation efficiency that is two times higher than the Gerchow *et. al*. [18] device. The interaction between positrons and matter, including positron tracking, was performed via GEANT and COMSOL simulation. Stainless steel was used for the construction of all of the flanges, tubes, and side walls of the chamber. In preparation for the application of a vacuum of 10^{-7} mbar, the chamber was cleaned, conditioned, and subjected to helium leak testing. Irradiation of 4 foils with dimension of 10×10 mm^2, thickness of 2 μm each, and purity of 99.6% was performed by stacking them in the irradiation holder.

A chamber that was used for the annealing of the tungsten foil (moderator) via the use of electron bombardment has been developed and constructed. The W foil was annealed in a vacuum level below 5×10^{-6} mbar at a temperature ~ 2050 ºC and was kept in 2 complete cycles in which the electron beam covered the entire foil.

It was demonstrated that the simulated results and the experimental ones are consistent, which results in the implementation of the improved magnetic bottle trap.

Bibliography

[1] C. D. Beling, S. Fung, L. Ming, M. Gong, and B. K. Panda, "Theoretical search for possible high efficiency semiconductor based field assisted positron moderators," *Appl. Surf. Sci.*, vol. 149, no. 1, pp. 253–259, Aug. 1999, doi: 10.1016/S0169-4332(99)00211-1.

[2] P. Coleman, *Positron Beams and Their Applications*. WORLD SCIENTIFIC, 2000. doi: 10.1142/3719.

[3] M. Charlton *et al.*, "Positron production using a 9 MeV electron linac for the GBAR experiment," *Nucl. Instruments Methods Phys. Res. Sect. A Accel. Spectrometers, Detect. Assoc. Equip.*, vol. 985, p. 164657, Jan. 2021, doi: 10.1016/j.nima.2020.164657.

[4] C. Hugenschmidt, G. Kögel, R. Repper, K. Schreckenbach, P. Sperr, and W. Triftshäuser, "First platinum moderated positron beam based on neutron capture," *Nucl. Instruments Methods Phys. Res. Sect. B Beam Interact. with Mater. Atoms*, vol. 198, no. 3–4, pp. 220–229, Dec. 2002, doi: 10.1016/S0168-583X(02)01527-6.

[5] J. Störmer, A. Goodyear, W. Anwand, G. Brauer, P. G. Coleman, and W. Triftshäuser, "Silicon carbide: A new positron moderator," *J. Phys. Condens. Matter*, vol. 8, no. 7, p. 89, 1996, doi: 10.1088/0953-8984/8/7/002.

[6] L. V. Jørgensen and H. Schut, "GaN-a new material for positron moderation," *Appl. Surf. Sci.*, vol. 255, no. 1, pp. 231–233, 2008, doi: 10.1016/j.apsusc.2008.05.200.

[7] N. Djourelov, A. Oprisa, D. Dinescu, and V. Leca, "Status of the project for a positron laboratory at ELI-NP," in *Journal of Physics: Conference Series*, Jan. 2017, vol. 791, no. 1, p. 012011. doi: 10.1088/1742-6596/791/1/012011.

[8] R. Zaleski, "Principles of positron porosimetry," *Nukleonika*, vol. 60, no. 4, pp. 795–800, 2015, doi: 10.1515/NUKA-2015-0143.

[9] P. Asoka-Kumar, M. Alatalo, V. J. Ghosh, A. C. Kruseman, B. Nielsen, and K. G. Lynn, "Increased Elemental Specificity of Positron Annihilation Spectra," *Phys. Rev. Lett.*, vol. 77, no. 10, p. 2097, Sep. 1996, doi: 10.1103/PhysRevLett.77.2097.

[10] F. Tuomisto, "Defect identification in semiconductors with positron annihilation : Experiment and theory," vol. 85, no. December, 2013, doi: 10.1103/RevModPhys.85.1583.

[11] J. Čížek, “Characterization of lattice defects in metallic materials by positron annihilation spectroscopy: A review,” *J. Mater. Sci. Technol.*, vol. 34, no. 4, pp. 577–598, Apr. 2018, doi: 10.1016/j.jmst.2017.11.050.

[12] H. Stoll, M. Koch, K. Maier, and J. Major, “Positron age-momentum correlation studies of defects and positronium by an MeV positron beam,” *Nucl. Inst. Methods Phys. Res. B*, vol. 56–57, no. PART 1, pp. 582–585, May 1991, doi: 10.1016/0168-583X(91)96101-P.

[13] N. G. Fazleev, M. P. Nadesalingam, W. Maddox, S. Mukherjee, K. Rajeshwar, and A. H. Weiss, “Oxidation and thermal reduction of the Cu(1 0 0) surface as studied using positron annihilation induced Auger electron spectroscopy (PAES),” *Surf. Sci.*, vol. 604, no. 1, pp. 32–37, Jan. 2010, doi: 10.1016/j.susc.2009.10.016.

[14] S. Legl and C. Hugenschmidt, “A novel time-of-flight spectrometer for PAES,” *Phys. status solidi c*, vol. 4, no. 10, pp. 3981–3984, Sep. 2007, doi: 10.1002/PSSC.200675802.

[15] N. Djourelov *et al.*, “POSITRON PRODUCTION BY GAMMA BEAM AT ELI-NP,” *Rom. Reports Phys.*, vol. 68, 2016.

[16] G. Li, W. Wang, and W. Yang, “Reports on Progress in Physics Prospects of III-nitride optoelectronics grown on Si Related content GaN-based light-emitting diodes on various substrates: a critical review,” *Rep. Prog. Phys*, vol. 76, p. 106501, 2013, doi: 10.1088/0034-4885/76/10/106501.

[17] D. Zhuang and J. H. Edgar, “Wet etching of GaN, AlN, and SiC: A review,” *Materials Science and Engineering R: Reports*, vol. 48, no. 1. Elsevier Ltd, pp. 1–46, Jan. 17, 2005. doi: 10.1016/j.mser.2004.11.002.

[18] L. Gerchow *et al.*, “High Efficiency Cyclotron Trap Assisted Positron Moderator,” *Instruments 2018, Vol. 2, Page 10*, vol. 2, no. 3, p. 10, Jun. 2018, doi: 10.3390/INSTRUMENTS2030010.

[19] “Nuclear Data.” http://nucleardata.nuclear.lu.se/ (accessed Jul. 22, 2021).

[20] C. Hugenschmidt, “Positrons in surface physics,” *Surface Science Reports*, vol. 71, no. 4. Elsevier, pp. 547–594, 2016. doi: 10.1016/j.surfrep.2016.09.002.

[21] C. Hugenschmidt *et al.*, “The Upgrade of the Neutron Induced Positron Source NEPOMUC,” *J. Phys. Conf. Ser.*, vol. 443, no. 1, p. 012079, Jun. 2013, doi: 10.1088/1742-6596/443/1/012079.

[22] C. Hugenschmidt *et al.*, “Unprecedented intensity of a low-energy positron beam,” *Nucl. Instruments Methods Phys. Res. Sect. A Accel. Spectrometers, Detect. Assoc. Equip.*, vol. 593, no. 3, pp. 616–618, Aug. 2008, doi: 10.1016/J.NIMA.2008.05.038.

[23] C. Hugenschmidt *et al.*, “Positron experiments at the new positron beam facility NEPOMUC at FRM II,” *Phys. status solidi c*, vol. 4, no. 10, pp. 3947–3952, Sep. 2007, doi: 10.1002/PSSC.200675757.

[24] H. Schut, A. van Veen, C. V. Falub, J. de Roode, and F. Labohm, “Performance of an Intense Nuclear-Reactor Based Positron Beam,” *Mater. Sci. Forum*, vol. 363–365, pp. 430–432, 2001, doi: 10.4028/WWW.SCIENTIFIC.NET/MSF.363-365.430.

[25] R. H. Howell, R. A. Alvarez, and M. Stanek, “Production of slow positrons with a 100-MeV electron linac,” *Appl. Phys. Lett.*, vol. 40, no. 8, pp. 751–752, Aug. 1982, doi: 10.1063/1.93215.

[26] C. Piochacz, “Generation of a High-brightness Pulsed Positron Beam for the Munich Scanning Positron Microscope,” 2009.

[27] N. Djourelov, A. Oprisa, and V. Leca, “Source of slow polarized positrons using the brilliant gamma beam at ELI-NP. Converter design and simulations,” 2015, doi: 10.1016/j.nima.2015.10.009.

[28] N. Djourelov, D. Dinescu, and V. Leca, “An overview of the design of ELIPS—A new slow positron beam line,” *Nucl. Instruments Methods Phys. Res. Sect. A Accel. Spectrometers, Detect. Assoc. Equip.*, vol. 934, pp. 19–25, Aug. 2019, doi: 10.1016/J.NIMA.2019.04.032.

[29] K. F. Canter, P. G. Coleman, T. C. Griffith, and G. R. Heyland, “Measurement of total cross sections for low energy positron-helium collisions. (Positron backscattering from metal surface),” *J. Phys. B At. Mol. Phys.*, vol. 5, no. 8, p. L167, Aug. 1972, doi: 10.1088/0022-3700/5/8/007.

[30] A. P. M. Jr., “Efficient generation of low-energy positrons,” *Appl. Phys. Lett.*, vol. 35, no. 5, p. 427, Aug. 2008, doi: 10.1063/1.91128.

[31] P. G. Coleman, T. C. Griffith, and G. R. Heyland, “A time of flight method of investigating the emission of low energy positrons from metal surfaces,” *Proc. R. Soc. London. A. Math. Phys. Sci.*, vol. 331, no. 1587, pp. 561–569, Jan. 1973, doi: 10.1098/RSPA.1973.0008.

[32] C. D. Beling, R. I. Simpson, M. Charlton, F. M. Jacobsen, T. C. Griffith, and P. Moriarty, “A Field-Assisted Moderator for Low-Energy Positron Beams,” vol. 116, pp. 111–116, 1987.

[33] C. D. Beling *et al.*, “A field-assisted moderator for low-energy positron beams,” *Appl. Phys. A 1987 422*, vol. 42, no. 2, pp. 111–116, Jan. 1987, doi: 10.1007/BF00616719.

[34] C. D. Beling, S. Fung, L. Ming, M. Gong, and B. K. Panda, “Theoretical search for possible high efficiency semiconductor based field assisted positron moderators,” *Appl. Surf. Sci.*, vol. 149, no. 1, pp. 253–259, 1999, doi: 10.1016/S0169-4332(99)00211-1.

[35] M. Shi, D. Gerola, W. B. Waeber, and U. Zimmermann, “Slow positron beam extraction from high magnetic fields,” *Appl. Surf. Sci.*, vol. 85, no. C, pp. 143–148, Jan. 1995, doi: 10.1016/0169-4332(94)00323-8.

[36] D. Gerola, W. B. Waeber, and M. Shi, “High efficiency positron moderation a feasibility study of the slow beam confinement extraction,” *Nucl. Instruments Methods Phys. Res. Sect. A Accel. Spectrometers, Detect. Assoc. Equip.*, vol. 364, no. 1, pp. 33–43, Sep. 1995, doi: 10.1016/0168-9002(95)00392-4.

[37] D. Gerola, W. B. Waeber, and M. Shi, “Design and simulation of the PSI electrostatic positron beam,” *Appl. Surf. Sci.*, vol. 85, no. C, pp. 106–110, Jan. 1995, doi: 10.1016/0169-4332(94)00317-3.

[38] J. Bardeen and W. H. Brattain, “The transistor, a semi-conductor triode [14],” *Physical Review*, vol. 74, no. 2. American Physical Society, pp. 230–231, Jul. 15, 1948. doi: 10.1103/PhysRev.74.230.

[39] P. P. Paskov and B. Monemar, “Optical Properties of III-Nitride Semiconductors,” in *Handbook of GaN Semiconductor Materials and Devices*, CRC Press, 2017, pp. 87–116. doi: 10.1201/9781315152011-3.

[40] B. Shen *et al.*, “III-nitride materials and characterization,” in *Handbook of GaN Semiconductor Materials and Devices*, CRC Press, 2017, pp. 3–52. doi: 10.1201/9781315152011.

[41] K. K. Schuegraf and K. Seshan, “Handbook of Thin Film Deposition Processes and

Techniques: Principles, Methods, Equipment and Applications," *Angew. Chemie*, vol. 101, p. 646, 2002.

[42] M. Ohring, *Materials Science of Thin Films: Deposition and Structure*. Academic Press, 2002.

[43] S. Duan *et al.*, "A density functional theory approach to mushroom-like platinum clusters on palladium-shell over Au core nanoparticles for high electrocatalytic activity," *Phys. Chem. Chem. Phys.*, vol. 13, no. 12, pp. 5441–5449, Mar. 2011, doi: 10.1039/C1CP20096H.

[44] S. A. Kukushkin, A. V Osipov, V. N. Bessolov, B. K. Medvedev, V. K. Nevolin, and K. A. Tcarik, "Substrates for epitaxy of Gallium Nitride:new materials and techniques," *Rev.Adv.Mater.Sci*, vol. 17, pp. 1–32, 2008.

[45] D. D. McNamara, "How do eclogites deform in subduction and collision zones? An Alpine study," 2009.

[46] H. Föll and B. O. Kolbesen, "Agglomerate von Zwischengitteratomen (Swirl-Defekte) in Silizium - Ihre Bedeutung für Grundlagenforschung und Technologie," in *Jahrbuch der Akademie der Wissenschaften in Göttingen*, 1976, p. 27. Accessed: Feb. 16, 2023. [Online]. Available: http://dtrinkle.matse.illinois.edu/MatSE584/articles/swirl/swirl.html

[47] A. Stolz *et al.*, "Optical waveguide loss minimized into gallium nitride based structures grown by metal organic vapor phase epitaxy," *Appl. Phys. Lett.*, vol. 98, no. 16, p. 161903, Apr. 2011, doi: 10.1063/1.3582055.

[48] D. Doppalapudi, E. Iliopoulos, S. N. Basu, and T. D. Moustakas, "Epitaxial growth of gallium nitride thin films on A-Plane sapphire by molecular beam epitaxy," *J. Appl. Phys.*, vol. 85, no. 7, p. 3582, Mar. 1999, doi: 10.1063/1.369718.

[49] T. Maruyama and H. Miyake, "Gallium nitride thin films deposited by radio-frequency magnetron sputtering," *J. Vac. Sci. Technol. A Vacuum, Surfaces, Film.*, vol. 24, no. 4, p. 1096, Jun. 2006, doi: 10.1116/1.2208988.

[50] F. E. Chen, "PLASMA PHYSICS AND CONTROLLED FUSION SECOND EDITION Volume 1: Plasma Physics," 1984.

[51] F. Yam, L. Low, S. Oh, Z. H.-O.-M. And, and U. 2011, "Gallium nitride: an overview of structural defects," in *Optoelectronics - Materials and Techniques*, 2011, pp. 99–136.

[52] S. Keller, H. Li, and M. Laurent, "GaN-based light-emitting diodes on various substrates : a critical review," *Reports Prog. Phys.*, p. 56501, doi: 10.1088/0034-4885/79/5/056501.

[53] C. William, M. L. Huggins, R. N. York, M. F. Roy, L. B. Clapp, and C. W. Mason, "Theory of X-ray Diffraction in Crystals (Zachariasen, William H.)," *J. Chem. Educ.*, vol. 22, no. 7, p. 364, Jul. 1945, doi: 10.1021/ED022P364.1.

[54] H. N. Southworth, "Scanning Electron Microscopy and Microanalysis," in *Physicochemical Methods of Mineral Analysis*, 2012, pp. 421–450. doi: 10.1007/978-1-4684-2046-3_11.

[55] C. A. Schneider, W. S. Rasband, and K. W. Eliceiri, "NIH Image to ImageJ: 25 years of image analysis," *Nature Methods*, vol. 9, no. 7. Nat Methods, pp. 671–675, Jul. 2012. doi: 10.1038/nmeth.2089.

[56] D. C. Palmer, "CrystalMaker." Begbroke, Oxfordshire, England, 2014.

[57] S. Amelinckx, D. van Dyck, J. van Landuyt, and G. van Tendeloo, *Handbook of Microscopy: Applications in Materials Science , Solid-state Physics and Chemistry*. VCH, 2008. doi: 10.1002/9783527620524.

[58] A. Bakhtazad and S. Chowdhury, "An evaluation of optical profilometry techniques for CMUT characterization," *Microsyst. Technol.*, vol. 25, no. 9, pp. 3627–3642, Sep. 2019, doi: 10.1007/s00542-019-04377-4.

[59] D. E. Eastman and M. I. Nathan, "Photoelectron spectroscopy," *Phys. Today*, vol. 28, no. 4, pp. 44–51, 1975, doi: 10.1063/1.3068920.

[60] C. Romanitan, I. Mihalache, O. Tutunaru, and C. Pachiu, "Effect of the lattice mismatch on threading dislocations in heteroepitaxial GaN layers revealed by X-ray diffraction," *J. Alloys Compd.*, vol. 858, p. 157723, Mar. 2021, doi: 10.1016/j.jallcom.2020.157723.

[61] L. Liu and J. H. Edgar, "Substrates for gallium nitride epitaxy," *Materials Science and Engineering: R: Reports*, vol. 37, no. 3. pp. 61–127, Apr. 30, 2002. doi: 10.1016/S0927-796X(02)00008-6.

[62] A. B. Șerban, V. L. Ene, C. C. Gheorghiu, D. Balabanski, E. Andronescu, and V. Leca, "RF magnetron sputtering of gallium nitride (GaN) on sapphire substrate," *UPB Sci. Bull. Ser. B Chem. Mater. Sci.*, vol. 81, no. 3, pp. 11–18, 2019.

[63] M. E. Lin, B. Sverdlov, G. L. Zhou, and H. Morkoç, "A comparative study of GaN epilayers grown on sapphire and SiC substrates by plasma-assisted molecular-beam epitaxy," *Appl. Phys. Lett.*, vol. 62, no. 26, pp. 3479–3481, Jun. 1993, doi: 10.1063/1.109026.

[64] A. Uedono *et al.*, "Behaviors of vacancy-type defects in Mg-implanted GaN during ultra-high-pressure annealing studied by using a monoenergetic positron beam," in *Gallium Nitride Materials and Devices XVI*, Mar. 2021, vol. 11686, p. 48. doi: 10.1117/12.2575972.

[65] H. Wu, Y. Sun, D. Lin, R. Zhang, C. Zhang, and W. Pan, "GaN nanofibers based on electrospinning: Facile synthesis, controlled assembly, precise doping, and application as high performance UV photodetector," *Adv. Mater.*, vol. 21, no. 2, pp. 227–231, 2009, doi: 10.1002/adma.200800529.

[66] S. Hautakangas, I. Makkonen, V. Ranki, M. J. Puska, K. Saarinen, and D. C. Look, "Direct evidence of impurity decoration of Ga vacancies in GaN from positron annihilation spectroscopy," pp. 1–4, 2006, doi: 10.1103/PhysRevB.73.193301.

[67] H. Hu *et al.*, "Boosted ultraviolet electroluminescence of InGaN/AlGaN quantum structures grown on high-index contrast patterned sapphire with silica array," *Nano Energy*, vol. 69, p. 104427, Mar. 2020, doi: 10.1016/j.nanoen.2019.104427.

[68] Z. Liliental-Weber, T. Tomaszewicz, D. Zakharov, J. Jasinski, and M. O'Keefe, "Defects in p-GaN and their atomic structure," in *IEEE Semiconducting and Semi-Insulating Materials Conference, SIMC*, 2005, vol. 2005, pp. 289–292. doi: 10.1109/SIM.2005.1511439.

[69] S. Zhou, X. Liu, H. Yan, Z. Chen, Y. Liu, and S. Liu, "Highly efficient GaN-based high-power flip-chip light-emitting diodes," *Opt. Express*, vol. 27, no. 12, p. A669, Jun. 2019, doi: 10.1364/oe.27.00a669.

[70] Z. Liliental-Weber, T. Tomaszewicz, D. Zakharov, J. Jasinski, and M. A. O'Keefe, "Atomic structure of defects in GaN:Mg grown with Ga polarity," *Phys. Rev. Lett.*, vol. 93, no. 20, Nov. 2004, doi: 10.1103/PhysRevLett.93.206102.

[71] B. Li *et al.*, “Magnetic and structural properties of Fe-implanted GaN at room temperature,” *Vacuum*, vol. 184, p. 109909, Feb. 2021, doi: 10.1016/j.vacuum.2020.109909.

[72] V. L. Ene *et al.*, “Study of Edge and Screw Dislocation Density in GaN/Al2O3 Heterostructure,” *Materials (Basel).*, vol. 12, no. 24, p. 4205, Dec. 2019, doi: 10.3390/ma12244205.

[73] V. L. Ene *et al.*, “Defect structure determination of GaN films in GaN/AlN/Si heterostructures by HR-TEM, XRD, and slow positrons experiments,” *Nanomaterials*, vol. 10, no. 2, Feb. 2020, doi: 10.3390/nano10020197.

[74] H. Lahrèche *et al.*, “Optimisation of AlN and GaN growth by metalorganic vapour-phase epitaxy (MOVPE) on Si(111),” *J. Cryst. Growth*, vol. 217, no. 1, pp. 13–25, Jul. 2000, doi: 10.1016/S0022-0248(00)00478-4.

[75] C. Romanitan, R. Gavrila, and M. Danila, “Comparative study of threading dislocations in GaN epitaxial layers by nondestructive methods,” *Mater. Sci. Semicond. Process.*, vol. 57, pp. 32–38, Jan. 2007, doi: 10.1016/j.mssp.2016.09.021.

[76] Reinhard Krause-Rehberg and Hartmut S. Leipner, *Positron Annihilation in Semiconductors - Defect Studies*, 1st ed. Springer-Verlag Berlin Heidelberg, 1999.

[77] A. B. Serban *et al.*, “Studies of Defect Structure in Epitaxial AlN/GaN Films Grown on (111) 3C-SiC,” *Nanomater. 2021, Vol. 11, Page 1299*, vol. 11, no. 5, p. 1299, May 2021, doi: 10.3390/NANO11051299.

[78] A. I. Williams *et al.*, “Moderation and diffusion of positrons in tungsten meshes and foils,” *J. Appl. Phys*, vol. 118, p. 105302, 2015, doi: 10.1063/1.4930033.

[79] O. G. De Lucio, M. Pérez, U. Mendoza, J. G. Morales, J. C. Cruz, and R. D. Dubois, “Study of tungsten based positron moderators,” *Nucl. Instruments Methods Phys. Res. Sect. B Beam Interact. with Mater. Atoms*, vol. 354, pp. 116–119, Jul. 2015, doi: 10.1016/j.nimb.2014.12.027.

[80] G. Street, “Studies of positron moderation in surface charged rare gas solids,” vol. 76, pp. 305–308, 1993.

[81] I. Ursu, L. Craciun, D. Niculae, and N. V. Zamfir, “The radiopharmaceuticals research center (CCR) of IFIN-HH at start,” *Rom. J. Phys.*, vol. 58, no. 9–10, pp. 1327–1336, 2013, Accessed: Oct. 15, 2022. [Online]. Available: https://www.researchgate.net/publication/269930884_The_radiopharmaceuticals_research_center_CCR_of_IFIN-HH_at_start

[82] F. Constantin, C. Barna, and P. Mereuta, “Positron annihilation spectroscopy studies of proton exchange membranes used in fuel cells,” *Polym. Adv. Technol.*, vol. 26, no. 12, pp. 1528–1530, Dec. 2015, doi: 10.1002/PAT.3575.

[83] G. Gibson, W. C. Jordan, and E. J. Lauer, “Containment of positrons in a mirror machine,” *Phys. Rev. Lett.*, vol. 5, no. 4, pp. 141–144, Aug. 1960, doi: 10.1103/PhysRevLett.5.141.

[84] J. Eades and L. M. Simons, “Deceleration in an anticyclotron as a means of producing very low energy antiprotons,” *Nucl. Instruments Methods Phys. Res. Sect. A Accel. Spectrometers, Detect. Assoc. Equip.*, vol. 278, no. 2, pp. 368–374, Jun. 1989, doi: 10.1016/0168-9002(89)90851-6.

[85] L. M. Simons, “Recent Results on Antiprotonic Atoms using a Cyclotron Trap at LEAR,” *Phys. Scr.*, vol. 1988, no. T22, p. 90, Jan. 1988, doi: 10.1088/0031-

8949/1988/T22/013.

[86] M. Shi, W. B. Waeber, D. Gerola, U. Zimmermann, and D. Taqqu, “Premoderation of positrons - Experiments on positron trapping and slowing-down,” *Nucl. Inst. Methods Phys. Res. A*, vol. 349, no. 1, pp. 8–14, Sep. 1994, doi: 10.1016/0168-9002(94)90601-7.

[87] N. Djourelov and A. B. Serban, “Optimization of a device for positron moderation based on a magnetic bottle,” *Nucl. Instruments Methods Phys. Res. Sect. A Accel. Spectrometers, Detect. Assoc. Equip.*, vol. 1014, p. 165699, Oct. 2021, doi: 10.1016/j.nima.2021.165699.

[88] S. Agostinelli *et al.*, “GEANT4 - A simulation toolkit,” *Nucl. Instruments Methods Phys. Res. Sect. A Accel. Spectrometers, Detect. Assoc. Equip.*, vol. 506, no. 3, pp. 250–303, Jul. 2003, doi: 10.1016/S0168-9002(03)01368-8.

[89] K. G. Lynn, B. Nielsen, and J. H. Quateman, “Development and use of a thin-film transmission positron moderator,” *Appl. Phys. Lett.*, vol. 47, pp. 239–240, 1985, doi: doi:http://dx.doi.org/10.1063/1.96231.

[90] *COMSOL Multiphysics®, COMSOL 4.3, COMSOL AB, Stockholm, Sweden, 2012.*

[91] A. Debelle, M. F. Barthe, and T. Sauvage, “First temperature stage evolution of irradiation-induced defects in tungsten studied by positron annihilation spectroscopy,” *J. Nucl. Mater.*, vol. 376, no. 2, pp. 216–221, May 2008, doi: 10.1016/j.jnucmat.2008.03.002.

[92] D. P. Verret and K. G. Ramanathan, “TOTAL HEMISPHERICAL EMISSIVITY OF TUNGSTEN.,” *J Opt Soc Am*, vol. 68, no. 9, pp. 1167–1172, Sep. 1978, doi: 10.1364/JOSA.68.001167.